Effects of pH and Ca exchange on the structure and redox state of synthetic Na-birnessite

Chiara Elmi[1,2,*], Jeffrey E. Post[1], Peter J. Heaney[3], Eugene S. Ilton[4]

[1]Department of Mineral Sciences, National Museum of Natural History, Smithsonian Institution, Washington, DC, 20013-7012, USA; [2]Current address: Department of Geology and Environmental Sciences, James Madison University, Harrisonburg, VA 22807, USA; [3]Department of Geosciences, Penn State University, 540 Deike Building, University Park, PA 16802, USA; [4]Pacific Northwest National Laboratory, 902 Battelle Blvd., Richland, WA 99352, USA

*Corresponding author: Chiara Elmi, elmicx@jmu.edu

Abstract. Birnessite-like minerals are among the most common Mn oxides in surficial soils and sediments, and they mediate important environmental processes (*e.g.*, biogeochemical cycles, heavy metal confinement) and novel technological applications (*e.g.*, water oxidation catalysis). Ca is the dominant interlayer cation in both biotic and abiotic birnessites, especially when they form in association with carbonates. The current study investigated the structures of a series of synthetic Ca-birnessite analogs prepared by cation-exchange with synthetic Na-birnessite at pH concentrations from 2 to 7.5. The resulting Ca-exchanged birnessite phases were characterized using powder X-ray diffraction and Rietveld refinement, Fourier transform infrared spectroscopy, Raman spectroscopy, X-ray photoelectron spectroscopy, and scanning and transmission electron microscopy. All samples synthesized at pH values greater than 3 exhibited a similar triclinic structure with nearly identical unit-cell parameters. The samples exchanged at pH 2 and 3 yielded hexagonal structures, or mixtures of hexagonal and triclinic phases. Rietveld structure refinement and X-ray photoelectron spectroscopy showed that exchange of Na by Ca triggered reduction of some Mn^{3+}, generating interlayer Mn^{2+} and vacancies in the octahedral layers. The triclinic and hexagonal Ca-birnessite structures described in this study were distinct from Na- and H-birnessite, respectively. Therefore, modeling X-ray absorption spectra of natural Ca-rich birnessites through a mixing of Na- and H-birnessite endmembers will not yield an accurate representation of the true structure.

INTRODUCTION

Phyllomanganates are highly reactive layer-structure Mn oxide minerals found in a wide variety of geological settings and are important constituents in soils and sediments. In particular, phyllomanganates having a birnessite-like structure readily participate in redox and cation-exchange reactions and exhibit high adsorption capacities for a variety of organic pollutants and toxic metallic ions (Le Goff et al. 1996; Manning et al. 2002; Feng et al. 2007; Lopano et al. 2007; Fleeger et al. 2013; Kwon et al. 2013; Shumlas et al. 2016). Layer Mn oxides have low point-of-zero charges (PZC) and therefore possess a relatively high negative charge at near-neutral pH values (Tan et al. 2008; Wang et al. 2010). Because of this high reactivity, phyllomanganates play an important role in controlling the concentration of trace metal ions in soils, sediments, and natural water systems (Post 1999; Tan et al. 2008). They also have been identified as promising heterogeneous compounds for water-oxidation catalysis (Sauer and Yachandra 2002; Feng et al. 2007; Jiao and Frei 2010; Wiechen et al. 2012; Frey et al. 2014).

Birnessite was first described by Jones and Milne (1956) as a natural phase discovered in Aberdeenshire, Scotland with a chemical formula of $Na_{0.7}Ca_{0.3}Mn_7O_{14} \cdot 2.8 \cdot H_2O$. Subsequently, numerous natural phases with “birnessite-like” structures have been described, including ranciéite (Post et al. 2008), takanelite (McKenzie 1971; Golden 1986), and lagalyite (Witzke et al. 2017). They commonly occur as fine-grained, poorly crystalline aggregates and coatings, making the studies of their structures and behaviors challenging. Additionally, various synthetic birnessite-like structures containing almost every alkali and alkaline earth element, as well as many of the transition metals, have been synthesized (*e.g.*, McKenzie 1971; Golden 1986) in attempts to elucidate the structural and chemical features of birnessite-like phyllomanganates (*e.g.*, Post and Veblen 1990; Kuma et al. 1994; Drits et al. 1997; Lanson et al. 2000; Post et al. 2003; Feng et al. 2004; Händel et al. 2013) and their reactivities (*e.g.*, Lanson et al. 2000; Manceau et al. 2002; Feng et al. 2007; Lopano et al. 2007, 2011; Wang et al. 2010, 2012; Landrot et al. 2012; Kwon et al. 2013; Lefkowitz et al. 2013, 2013; Yin et al. 2013; Fischel et al. 2015; Hinkle et al. 2016; Zhao et al. 2016; Fischer et al. 2018). Laboratory studies have also demonstrated that formation of birnessite-like phases can be initiated, or enhanced, by certain microbes and fungi (Tebo et al. 2004; Webb et al. 2005; Grangeon et al. 2010; Santelli et al. 2011), and it is therefore likely that biologically mediated phyllomanganates are important in natural systems.

The birnessite structure is constructed of stacked layers of nominally Mn^{4+}-O_6 octahedra; substitution of Mn^{3+} or other lower valence cations and/or vacancies for Mn result in a net negative charge on the octahedral sheets (Fig. 1). The charge is offset by addition of large uni- or divalent cations (*e.g.* Na^+, Ba^{2+}, K^+, Ca^{2+}) into the interlayer region, along with water molecules. Birnessite-like phases with predominantly Mn^{4+} exhibit overall hexagonal (trigonal) or near-hexagonal symmetry. As the proportion of Mn^{3+} increases, the associated Jahn-Teller distortions lower the symmetry to triclinic (Silvester et al. 1997; Ling et al. 2018). Birnessite-like structures exhibit a characteristic ~7 Å repeat in the layer stacking direction. In buserite phases, a double layer of water molecules expands the layer spacing to ~10 Å. Recent studies of naturally occurring birnessite/buserite-like phases from fresh-water environments revealed Ca to be the predominant interlayer cation, sometimes associated with Mg, Ba, and/or K (Bargar et al. 2005; Tan et al. 2010).

It is generally assumed that naturally occurring Ca-rich phyllomanganates form by a biologically mediated, or enhanced, process (Bargar et al. 2005). Interestingly, the water-oxidation reaction that is a critical step in photosynthesis is catalyzed within the enzyme photosystem II (PSII) by a μ-oxido bridged $CaMn_4$ cluster known as the oxygen-evolving-complex (OEC) (Umena et al. 2011; Zhang et al. 2015; Yamaguchi et al. 2017). Inspired by the composition of the OEC, scientists have explored the water-oxidation capacity ofranciéite, the Ca-rich member of the birnessite group (Sauer and Yachandra 2002; Andreiadis et al. 2011; Hou 2011; Wiechen et al. 2012; Frey et al. 2014; Zaharieva et al. 2016). Some of these water-oxidation experiments demonstrated that birnessite-like minerals require the presence of calcium in their structures to reach maximum catalytic activity (Wiechen et al. 2012).

Because of the widespread association of Ca with natural phyllomanganates and the critical role of birnessite-like clusters in water-oxidation catalysis, we undertook an investigation of interactions of aqueous Ca with synthetic birnessite-like phases. A primary goal of the study was to explore the chemical and structural modifications occurring in synthetic Na-birnessite when transformed by cation exchange into Ca-birnessite in aqueous solutions over a range of pH and Ca concentrations that are similar to those found in many natural systems. In particular, this paper aims to determine whether the Ca-birnessite structure is distinct from other varieties of birnessite, and to gain insights into the mechanism(s) by which cation-exchange transforms birnessite-like structures. Additionally, the synthesized Ca-birnessites are compared with natural Ca-rich birnessite-like phases, including ranciéite.

MATERIALS AND METHODS

Synthesis of Na-birnessite and hexagonal birnessite

Triclinic birnessite was prepared following the synthesis for Na-birnessite outlined in Lopano et al. (2007), based on the synthesis procedures described by Golden (1986). In the present synthesis, 250 ml of 5.5 *M* NaOH solution and 200 ml of 0.5 *M* $MnCl_2 \cdot 4H_2O$ solution were chilled overnight at 4 ºC. The Na-birnessite precipitate was formed by stirring the NaOH and $MnCl_2 \cdot 4H_2O$ solutions at room temperature and then bubbling oxygen into the mixture with a Pyrex^{TM} coarse porosity fritted cylinder (pore size = 40-60 μm) for five hours. Analytical grade chemicals and deionized water were used for the synthesis. The precipitate was centrifuged in conical polypropylene centrifuge tubes (capacity = 50 ml) and rinsed five times with 40 ml of deionized water. The sample was then left to air-dry on a watch glass at room temperature overnight. After 24 hours, the sample was dried at 30 ºC for 5 minutes to effect a complete transformation from Na-buserite to Na-birnessite.

Hexagonal birnessite was synthesized by reacting ~100 mg of dried triclinic Na-birnessite in 250 ml of 0.001 *M* HCl for 24 hours. The sample was then centrifuged 5 times with deionized water, and left to air-dry overnight. Previous studies have shown, and our EDS analyses confirmed, that the hexagonal birnessite had no Na, or metal cations other than Mn, in the structure.

Ca- exchange experiments

100 mg samples of triclinic Na-birnessite were placed in 600 ml glass beakers with 200 ml of 1 *M*, 0.1 *M*, and 0.01 *M* $CaCl_2 \cdot 2H_2O$ solutions initially at pH 6.5 and pH 7.5 for ~24 h. Analytical grade chemicals and deionized water were used for the Ca exchange experiments. The beakers were covered with Parafilm® for the duration of the experiments. After 24 hours, each Ca-exchanged sample was centrifuged in conical polypropylene centrifuge tubes (capacity = 50 ml) and rinsed five times with 40 ml of deionized water. The samples were then air-dried on a watch glass at room temperature overnight, and then dried at 30 ºC for 5 minutes to effect a complete transformation from Ca-buserite to Ca-birnessite. In order to monitor the rate of the cation exchange, sample aliquots were removed from the reaction vessel at 5 min intervals for the first hour and then every hour until the end of the run for the experiment at pH 6.5 using 1 *M* Ca^{2+}.

The exchange experiments were repeated following the same procedure above at pH 5.5, pH 4, pH 3 and pH 2. In these experiments, the initial pH of Ca solutions was adjusted with 0.1 *M* HCl; the pH of the reaction solution was also measured at the end of each exchange experiment. For all exchange reactions other than at pH 3, the final pH increased by less than 0.5 units; the final values for the exchanges at pH 3 ranged between 4.9 and 5.6.

Scanning electron microscopy

Uncoated Ca-birnessite samples were mounted on carbon tape adhered to an aluminum stub and analyzed with scanning electron microscopy (SEM) using a field emission source (FEI Apreo) equipped with an EDAX Octane Silicon Drift energy-dispersive X-ray spectroscopy (EDS) detector (Scanning Electron Microscopy Laboratory, National Museum of National History, Smithsonian Institution). Backscattered electron (BSE) images were collected, and energy dispersive X-ray spectroscopy (EDS) was used to determine the chemical composition and homogeneity of the Ca-birnessite samples (with beam current of 1.6 nA). The images were collected and analyses performed in low vacuum (0.31 torr) at an accelerating voltage of 15 kV. The data were processed using the Noran System Six 3 (NSS 3) software.

X-ray diffraction (XRD)

All prepared samples were characterized by powder X-ray diffraction using a Rigaku II D/MAX-RAPID microdiffractometer (Smithsonian Institution, Department of Mineral Sciences) equipped with a graphite monochromator and a curved image plate area detector. A Mo tube (50 kV, 40 mA) was used as the X-ray source with a 0.3 mm collimator. Small (~1 mm) balls of sample were mounted with water-based glue on tips of glass fibers, and during exposure to the X-ray beam, the sample was oscillated between -30º to +30º phi to minimize the effects of sample heterogeneity and preferred orientation. The full set of Debye-Scherrer diffraction rings from the imaging plate data were integrated using Rigaku-provided software, and interpretation of XRD patterns was performed using the JADE 9 software package. Additionally, synchrotron XRD data sets for selected samples (pH: 7.5, 6.5, 3, and 2) were collected at the Advanced Photon Source (Beam Line 13-BM-C) for samples mounted in 1 mm (ID) polyimide capillaries using 30 s exposures with a MAR CCD 165 area detector and $\lambda = 0.828438$ Å. The synchrotron image data were processed to 2D intensity-versus-2Theta patterns using Dioptas (Prescher and Prakapenka 2015).

Rietveld refinements (Rietveld, 1969) were performed for selected samples using the General Structure Analysis System-II (GSAS-II) software (Toby and Von Dreele 2013). Diffraction data generated by a LaB_6 standard (NIST SRM 660a) were used to calibrate peak profile parameters that described instrumental broadening for the Rigaku and synchrotron experiments. For all samples, diffraction peak profiles were fit with a pseudo-Voigt function as parameterized by Thompson, et al. (1987), with asymmetry correction by Finger et al. (1994), and microstrain anisotropic broadening terms by Stephens (1999).

The structure refinements were initiated using the triclinic Na- birnessite structure of Lopano et al. (2007), and the starting atom positions for the H-birnessite refinement were derived from Ling et al. (2015). The (001) peak was omitted due to its high relative intensity and problems with integrating the diffraction images near the direct beam. The background parameters, scale factor, unit-cell parameters, peak profile coefficients, and appropriate atom parameters were allowed to vary. The background intensities were fitted with a Chebyshev function using 5-7 terms.

Transmission electron microscopy (TEM)

Samples of Ca-birnessite formed from exchange of triclinic Na-birnessite with solutions containing 1.0 and 0.1 M Ca^{2+} at pH 2 and 0.1 M Ca^{2+} at pH 7.5 were prepared for TEM analysis by lightly grinding powders in ethanol in an agate mortar to disaggregate the particles. The ethanol-birnessite suspension then was ultrasonicated for 60 s, followed by immersion of a holey carbon TEM grid into the suspension. The grain mounts were analyzed using a ThermoFisher Scientific Talos F200X TEM with a field-emission gun (FEG) source operating at 200 kV in the Materials Characterization Laboratory at Penn State University.

FT-IR spectroscopy

Transmission spectra of the Na-, H-, and Ca-birnessite samples were obtained at room temperature over the range 350–6000 cm^{-1} using a Thermo Scientific Nicolet 6700 Fourier-Transform infra-red spectrometer (Smithsonian Institution, Department of Mineral Sciences). KBr pellets were prepared from mixtures of approximately 1 mg of Mn oxide and 250 mg of KBr that were ground in a mill for at least 1 min, and pressed for 2 min. The resolution was set at 3.86 cm^{-1}, and 120 scans were co-added for each spectrum. During data collection, the sample chamber was purged with air scrubbed for water and CO_2. Background spectra for samples did not show significant shifts over time. The Omnic 8 software (Nicolet) was used for data collection.

Raman spectroscopy

Raman spectra for the Na-, H-, and Ca-birnessite samples were collected using a HORIBA LabRam HR Evolution equipped with deep-depleted thermoelectrically cooled CCD (charge coupled device) array detector and an optical microscope (Smithsonian Institution, Department of Mineral Sciences). All measurements were made at 25 °C. All powders were pressed onto glass discs to obtain an approximately flat surface for Raman analysis. Sample areas were analyzed using an Olympus 50× objective, an integration time of 30 s, and at a spectral resolution of 2 cm^{-1} using a 784 nm solid state laser. Four acquisitions per spot were set to improve the signal-to-noise ratio. Low laser power was used to minimize sample alteration by heating. The spectrometer was fitted with a holographic notch filter and grating (600 g/mm), and was controlled using the Horiba LaBSPEC6 software.

X-ray photoelectron spectroscopy (XPS)

XPS analyses were performed to determine concentrations of Mn^{4+}, Mn^{3+}, and Mn^{2+} for Ca-birnessite samples exchanged using 0.01 M Ca^{2+}at pH 7.5, 3, and 2. Because of limited instrument availability, samples were selected that represented the range of pH conditions and different structure symmetries. Data collection and fitting procedures were followed as reported by Ilton et al. (2016). Powder samples were covered with a strip of conductive copper tape and pressed with clean borosilicate glass blocks onto copper stubs. XPS measurements were performed with a Physical Electronics Quantera Scanning X-ray Microprobe. This system uses a focused monochromatic Al Kα X-ray (1486.7 eV) source for excitation and a spherical section analyzer. The instrument has a 32 element multichannel detection system. The X-ray beam is incident normal to the sample and the photoelectron detector is at 45° off-normal. High energy resolution spectra were collected using a pass-energy of 69.0 eV with a step size of 0.125 eV. For the Ag $3d_{5/2}$ line, these conditions produced a FWHM of 0.92 eV ± 0.05 eV. The binding energy (BE) scale is calibrated using the Cu $2p_{3/2}$ feature at 932.62 ± 0.05 eV and Au $4f_{7/2}$ at 83.96 ± 0.05 eV. The sample experienced variable degrees of charging. Low energy electrons at ~1 eV, 20μA and low energy Ar^+ ions were used to minimize this charging. Measurements of the Mn*2p*, Mn*3s*, Mn*3p*, O*1s*, C*1s*, and various alkali and alkaline Earth lines were conducted with a step size of 0.1 eV, an analysis area of 300 × 700 μm, and pass energies (PE) of 20 or 40 eV. The low sensitivity of the Mn*3s* line resulted in measurements only with PE = 40 eV. Survey scans were conducted at PE = 160 eV and step size = 0.5 eV. XPS spectra were fit by non-linear least squares after Shirley background subtractions with the CasaXPS curve resolution software package. Gaussian/Lorentzian contributions to line shapes were numerically convoluted with a Voigt function.

RESULTS

SEM and EDS Analyses

SEM images (Fig. 2) show that all of the Na-birnessite and Ca-exchanged birnessite samples exhibited the same flake-like morphology. Morphology and crystal size (~2 μm in diameter) did not change significantly from the starting Na-birnessite following exchange at different Ca concentrations and pH conditions.

The EDS analyses confirmed that the exchange of Ca for Na was complete for all samples within detection limits for Na (nominally 0.05 wt.%). The degree of Ca uptake as a function of pH and Ca^{2+} concentration is displayed in Figure 3. For experiments at pH 4 and above, the number of Ca cations exchanged per Mn atom was approximately half that of Na in the starting Na-birnessite (from ~0.30 Na/Mn to ~0.16 Ca/Mn), as expected for a charge-neutral exchange, *i.e.* one Ca^{2+} for every 2 Na^+. Moreover, the exchange of Ca for Na was rapid. EDS analyses revealed that full exchange had occurred within 5 min after Na-birnessite powders were added to a 1 *M* Ca^{2+} solution at pH 6.5. In contrast, birnessite samples exchanged at pH 2 and 3 exhibited lower levels of exchange (except at pH 3 when the Ca^{2+}_{aq} concentration was ≥1 *M*). In solutions at pH 3 and with 0.1 *M* and 0.01 *M* Ca^{2+} − and for all concentrations of Ca^{2+}_{aq} prepared at pH 2 − the number of Ca cations per Mn atom was approximately 1/3 of that for the samples exchanged at higher pH (~0.05 Ca/Mn rather than ~0.16 Ca/Mn) (Fig. 3).

XRD and Rietveld Refinements

The powder XRD patterns for products from 1 M Ca-exchange experiments at various pH values are plotted in Figure 4, and they indicate similar triclinic structures for all pH values greater than 2. Rietveld refinements for our synthetic Na- and H-birnessite endmembers yielded structures and unit-cell parameters consistent with those previously reported (Post et al. 2002; Ling et al. 2015). On the other hand, when Ca^{2+} exchanged in a 1:2 ratio with Na^+ at pH 3 to 7.5, the X-ray diffraction patterns for the resulting Ca-birnessite differed sufficiently from those of Na-birnessite that a new unit cell was required for Rietveld analysis. Viable unit-cell parameters for these Ca-birnessite samples were ascertained using the computer program Crystal Cracker (Leinenweber, 2019), and confirmed by performing a successful LeBail fit using GSASII. For the initial stages of refinement for these Ca-birnessite samples, only the octahedral Mn and O atoms were included in the structure model. Difference Fourier maps were calculated for the interlayer region to locate electron density corresponding to H_2O/Ca molecules.

For all structures that experienced a 1:2 Ca^{2+}:Na^+ exchange, the difference maps revealed significant electron density within the interlayer near z = 0.6 (and by symmetry, z = 0.4). The location and the diffuse nature of the electron density suggested that it corresponded to a disordered Ca/H_2O position. There was a lesser area of electron density centered at approximately (0, 0, 0.66) that might arise from Ca coordinated to the octahedral sheets (*i.e.*, above and below possible Mn vacancies), as occurs in natural ranciéite (Post et al. 2008). The observed H_2O/Ca site was added to the structure model (as O), and its position and occupancy factor were allowed to vary during subsequent refinement cycles. A Ca site was added that corresponded to the electron density peak on the difference map at (0, 0, 0.66); attempts to refine an occupancy factor did not yield consistent results, most likely because of the low occupancy (~0.07, assuming 7% Mn vacancies and consistent with the measured XPS Mn^{2+} composition) and strong correlations in the refinement between the occupancy factor and background coefficients. Consequently, the Ca site occupancy factor was fixed to a value of 0.07. The refined unit-cell parameters for Ca-birnessite samples synthesized under a range of pH and Ca^{2+}

concentration conditions are listed in Table 1. A structure drawing for synthesized Na- and Ca-birnessite is shown in Figure 1.

Rietveld refinements for all structures that experienced a 1:2 Ca^{2+}:Na^{+} exchange yielded triclinic unit cells that are significantly different from that of Na-birnessite, but nearly identical to each other. On the other hand, samples exchanged at pH 3 using 0.1 *M* and 0.01 *M* Ca^{2+} were mixtures of a predominantly hexagonal phase and a minor triclinic phase (Table 1). The structure for samples exchanged with 0.01 *M* Ca^{2+} at pH 2 was refined using a hexagonal unit cell in space group *P*-3 (Fig. 1), closely similar to that of hexagonal H-birnessite Ling et al. (2015). At pH 2 and higher concentrations of dissolved Ca^{2+} (1.0 and 0.1 *M* Ca^{2+}), however, refinements required a triclinic cell, but one in which the *a* and *b* unit-cell parameters matched those of hexagonal H-birnessite, but the values for the α and β unit-cell angles did not. The final Rietveld refinement difference plot reveals an additional peak at d ~ 1.86 Å. It is weaker or absent in other preparations at similar pH conditions. The peak could be an impurity not related to the Ca-birnessite structure. Final observed and calculated diffraction patterns for representative Rietveld refinements for triclinic and hexagonal structures are shown in Figure 5.

FTIR and Raman spectra

Ling et al. (2017) demonstrate that FTIR spectroscopy can successfully differentiate triclinic from hexagonal birnessites. FTIR spectra of triclinic Na-birnessite show three distinct peaks in the Mn-O vibrational mode region, but only two modes are obvious for the higher symmetry hexagonal, or near-hexagonal, structures. Likewise, Raman spectra for triclinic and hexagonal birnessites show differences in the number and positions of peaks (Julien 2003; Hsu et al. 2011; Yang et al. 2015; Boumaiza et al. 2019). FTIR (Fig. 6) and Raman (Fig. 7) spectra for several of the Ca-birnessite samples prepared in this study show clear trends as a function of solution pH. The FTIR and Raman spectra for Ca-birnessite samples that underwent a 1:2 Ca^{2+}:Na^{+} exchange at higher pH were similar to that of Na-birnessite, whereas those prepared at lower Ca^{2+} concentrations at pH 3 and all samples at pH 2 were analogs to that of H-birnessite. Consequently, the FTIR and Raman results reinforce our conclusions based on X-ray diffraction – that fully exchanged Ca-birnessites at higher pH are triclinic, whereas Ca-birnessites exchanged at low pH are hexagonal, or nearly so.

HRTEM and SAED

High-resolution TEM and selected-area election diffraction also supported the conclusion that Ca-birnessite crystals synthesized at higher pH and Ca concentrations were structurally distinct from those produced at pH 2. Ca-birnessite samples generated from the reaction of triclinic Na-birnessite with solutions at pH 2 and either 0.1 or 1 *M* $CaCl_2$ exhibited SAED patterns with hexagonal symmetry (Z.A. [001]) that typically were free of streaks or superstructures (Fig. 8A,B). High-resolution TEM images of these crystals (Fig. 8) generally exhibited little in the way of microstructural defects, although faint superstructure reflections halfway along the [100]* and [010]* directions were apparent, suggesting a doubled superperiodicity involving the 100 and 001 planes in local areas (Fig. 8C). Rarely, crystals with heavy structural disorder were observed, as evidenced by streaking in SAED patterns and irregular modulations among the (100) and (010) planes in HRTEM images.

In contrast, TEM analysis of Ca-birnessite crystals exchanged from Na-birnessite at pH 7.5 revealed a structural character that was more closely analogous to that of triclinic birnessite. The angle between [100]* and [010]* deviated sufficiently from hexagonality that superimposition of the same SAED pattern on itself with a 60° rotation yielded a clear doubling of diffraction spots. Consequently, these diffraction patterns were best indexed to the $C\bar{1}$ cell (Fig. 9A,B). Additionally, these crystals commonly revealed superstructure reflections at 1/3 [200]*, as was also observed in SAED patterns of the starting triclinic Na-birnessite but never in our hexagonal birnessite. HRTEM images and fast-Fourier transforms of these triclinic crystals likewise displayed stronger superperiodicities and streaking than were observed in the hexagonal birnessites prepared at pH 2 (Fig. 9C).

XPS

Following Ilton et al. (2016), the 3*p* XPS spectra were fitted to determine the Mn oxidation state concentrations for Ca-birnessite samples exchanged using 0.01 M Ca^{2+}at pH 7.5, 3, and 2. Ilton et al. (2016) conclude that the 3*p* data are most representative of the bulk sample and yield results that best match those for Mn oxide standards. The Mn oxidation states determined for the samples measured in this study are given in Table 2. Interestingly, the average oxidation states for the phases in Table 2 are not significantly different, despite major changes in the relative abundances of the different Mn oxidation states. The relatively large estimated errors for the pH 3 values can be attributed to the observation that this sample was a mixture of triclinic and hexagonal phases, as discussed below. Relationships between $Mn^{2+,3+}$ content and structural symmetry are plotted in Figure 10.

DISCUSSION

Effects of Ca substitution on the triclinic birnessite structure

Variations among triclinic unit cells of birnessite. The crystal structures for Ca-birnessite samples exchanged above pH 3 for all Ca^{2+} concentrations are triclinic, and they are similar to each other but different from that of Na-triclinic birnessite, as is the Ca-birnessite produced at pH 3 and 1 *M* Ca^{2+}. The unit-cell parameters determined by the Rietveld refinements for these triclinic Ca-birnessite phases were identical within experimental error. Similarly, the analyzed Ca concentrations for these Ca-birnessite samples were essentially the same, with Ca/Mn = 0.16 (Fig. 3), indicating a 1:2 charge-balanced exchange of Ca^{2+} for Na^{+}. Moreover, when Na-birnessite samples were immersed in pH 6.5 solutions at 1 *M* Ca^{2+} and analyzed by XRD at 5-min intervals during the exchange reaction for 1 hr, the unit-cell parameters exhibited no measurable changes with time. These observations strongly support the existence of a triclinic Ca-birnessite structure that is distinct from other triclinic varieties of birnessite. Specifically, the unit-cell lengths and angles refined here reveal a markedly smaller deviation from hexagonal symmetry than is the case with Na-, K-, or Ba-birnessite (Table 1), consistent with the inferences of Ling et al. (2018). We hypothesize that this structure may closely correspond to natural triclinic Ca-birnessites that form at circumneutral pH and a range of Ca concentrations.

Previous studies have shown that cation exchange of K, Mg, Ba, Cs, and Li for Na in triclinic birnessite produce distinctly different triclinic unit cells (Chukhrov et al. 1979; Golden 1986; Lopano et al. 2007; Fleeger et al. 2013). The refined crystal structures reported for these birnessites exhibit similar *a* and *b* unit-cell parameters, suggesting that the Mn-O octahedral sheets are relatively undistorted by the interlayer cations when they reside in the middle of the interlayer ($z \sim 0.5$). Rather, hydrated cations of different sizes, charges, and occupancies are accommodated primarily through minor translations of neighboring octahedral sheets, as is reflected in differences in unit-cell angles and layer spacings (the *c*-axis length) (Table 1).

Mn reduction induced by Ca exchange. Although our refinement of triclinic Na-birnessite revealed full occupancy for octahedral Mn (as is consistent with previous reports), all of the triclinic Ca-birnessite analyses in the present study yielded octahedral vacancies ranging from 3 to 10%, with an average of 7%. The variations exhibited for the Mn occupancy factor did not correlate with differences in experimental conditions, but likely represent uncertainties in the Rietveld results because of correlations among the Mn occupancy factor, background coefficients, and thermal parameters. These non-unitary occupancies suggest that concomitant with the exchange of Ca for Na is a loss of some Mn from the octahedral sheets, most likely by reduction of some Mn^{3+} to Mn^{2+}, which goes into solution. This scenario is in agreement with Kong (2017), who showed the release of Mn into solution following exchange of 1.0 *M* Ca^{2+} with Na-birnessite at near neutral pH. Additionally XPS analyses of the Ca-birnessite sample exchanged from Na-birnessite at pH 7.5 using 0.1 *M* Ca^{2+} showed a decrease in the Mn^{3+}/Mn^{4+} value, relative to that of Na-birnessite, from 0.61 (Ilton et al. 2016) to 0.45. The XPS data also indicate that ~7% of the total Mn is Mn^{2+}, which might be absorbed onto the surface, and/or in the interlayer with the Ca.

The FTIR and Raman spectra (Figs. 6 and 7) provide additional support for the interpretation that Mn^{3+} and/or Mn^{4+} are reduced during Ca exchange with Na-birnessite. The Raman and FTIR spectra for samples exchanged at pH values greater than 3.0 are consistent with those for triclinic birnessite phases (Ling et al. 2017). One notable difference, however, is a ~12 nm shift of the Mn-O stretch Raman line at ~650 nm to higher wavenumbers following exchange of Ca with Na-birnessite. Our observations comparing Raman spectra for several well-characterized phyllomanganate phases suggest that the ~650 nm Raman line shifts to lower wavenumbers with increasing values of Mn^{3+}/Mn^{4+}, presumably as a consequence of the longer average Mn^{3+}-O bonds relative to those with Mn^{4+}. The Raman spectra shown here, therefore, are consistent with a decrease in Mn^{3+}/Mn^{4+} as Ca exchanged for Na, and the magnitude of the shift is essentially the same for all of the triclinic Ca-birnessite samples.

Maintaining charge balance. How is charge balance achieved in the birnessites that experienced a 1:2 Ca^{2+}:Na^{+} exchange? If we adopt an average occupancy of 0.93 for octahedral Mn, as was typical of our refinements, then 7% of the octahedral sites are vacant ($\square_{occ} = 0.07$). If we further accept the XPS-derived Mn^{3+}/Mn^{4+} value of 0.45 (Mn^{3+}= 29%, Mn^{4+}= 64%, and Mn^{2+} = 7%), then $Mn^{3+}{}_{occ} = 0.29$ and $Mn^{4+}{}_{occ} = 0.64$. Since the multiplicity of Mn in S.G. *C*-1 is 2, that leads to 0.14 vacancies per unit cell and 0.58 Mn^{3+} cations per unit cell. Pauling's second rule shows that an octahedral sheet fully occupied by Mn^{4+} is charge balanced [3 x 4/6 = 2]. Therefore, the charge deficit caused by substitutions of either vacancies or Mn^{3+} cations for Mn^{4+} yields a net negative charge per unit cell. Since triclinic birnessite has one octahedral sheet per unit cell, summing the charge deficits in Ca-birnessite [(-4) × 0.14 for $\square$ plus (-1) × 0.58 for Mn_{oct}^{3+}] yields a negative charge of -1.22 for each octahedral sheet. This calculation assumes that Mn^{2+} cations are too large to occupy the octahedral sites (Post 1999), and it does not consider that some of the Mn^{3+} might be in interlayer sites.

Do the measured concentrations of interlayer cation content accommodate the negative sheet charge? EDS analyses for the birnessites exchanged at higher pH yielded 0.15 Ca/Mn (Fig. 3) for a contribution of +0.60 per unit cell, and XPS analyses indicated ~0.14 Mn^{2+} for a contribution of +0.28 per unit cell for a total charge of ~ +0.88 per unit cell. The charge discrepancy between sheet and interlayer might suggest that interlayer Mn^{3+} or H_3O^{+} occupies interlayer sites and/or that OH^{-} replaces some of the O atoms in the octahedral sheets. If we assume that no Mn^{2+} was lost to solution, that no Mn^{3+} resides in the interlayer, and that H^{+} in some fashion balances the octahedral charge deficit, then the resulting formula for this Ca-exchanged birnessite at pH 7.5 is $(Ca^{2+}_{0.15}, Mn^{2+}_{0.07}, H^{+}_{0.13}) (Mn^{3+}_{0.29}, Mn^{4+}_{0.64}, \square_{0.07}) O_2 \cdot xH_2O$. In comparison, the formula for the starting Na-birnessite before exchange was approximately $(Na^{+}_{0.29}, Mn^{2+}_{0.02,} H^{+}_{0.06}) (Mn^{3+}_{0.39}, Mn^{4+}_{0.61}) O_2 \cdot 0.75H_2O$.

These calculations suggest that some of the divalent cations occupy positions near the center of the interlayer. The negative charge induced by 0.14 vacancies per octahedral sheet in Ca-birnessite would be balanced by 0.28 (Ca^{2+} + Mn^{2+}), which is a little more than half that determined by EDS and XPS analyses, which yielded ~0.30 Ca^{2+} and 0.14 Mn^{2+}, respectively, per unit cell. Alternatively, some of the vacancies might be compensated by Mn^{3+}.

The fact that the average 0.14 vacant octahedral sites per unit cell determined by our refinements is equal to the 0.14 Mn^{2+} per unit cell measured by XPS suggests the possibility that all of the Mn that moved into the interlayer as Mn^{2+} are located above and below the resulting vacancies. Any remaining interlayer cations likely occupy positions closer to the middle of the interlayer region where they are coordinated to water molecules and octahedral O atoms. Because of the positional disorder and diffuse electron density, it is not clear how meaningful is the occupancy factor refined for the interlayer Ca/H_2O site, but the value is sufficiently large to more than account for what would be predicted if it is fully occupied by H_2O molecules and all of the Ca^{2+} cations. The precise positions of these Ca^{2+}, and possibly some Mn^{2+}, or Mn^{3+}, cations near z = 0.5-0.6 in the interlayer might correlate to the local arrangement of Mn^{3+} and vacancies in the adjacent octahedral sheets. Our refinements offered no indications for long-range order of either the octahedral vacancies or Mn^{3+} cations, and the diffuse electron densities revealed in difference Fourier maps suggest positional disorder among the interlayer cations and water molecules.

Effects of Ca substitution on the hexagonal birnessite structure

Increasing hexagonality with increasing H^+:Ca^{2+} ratios. The final products of the exchange reactions at pH 2 and 3 depended upon the pH and the Ca^{2+} concentration. For the exchanges with 0.1 *M* Ca^{2+} at pH 3, the XRD and Raman data revealed a mixture with approximately 1/3 triclinic and 2/3 hexagonal birnessite structures, based on Rietveld refinement. The unit-cell parameters for the two phases are listed in Table 1. The Ca-birnessite formed using 0.01 *M* Ca at pH 3 was similarly mixed, but with only ~25% triclinic Ca-birnessite. However, all of the Ca-birnessites produced at pH 2 exhibited hexagonal, or near hexagonal, symmetries, according to our XRD, FTIR, Raman, and TEM analyses. Interestingly, the Rietveld refinement for the sample exchanged using 0.1 *M* Ca^{2+} yielded an excellent fit for a structure with *a, b,* and *c* unit-cell parameters similar to those for hexagonal H-birnessite, but the α angle in particular (94.25°) differed from the expected value of 90° (Table 1). Apparently, the Mn-O octahedral sheets in this Ca-birnessite structure have near-hexagonal symmetry, consistent with the observed *a*, *b*, and γ values, but the stacking of the sheets gives rise to triclinic symmetry. The hexagonal symmetry indicated by the Raman spectrum for this sample (Fig. 5) is consistent with that of the average local environment around Mn in the octahedral sheet.

The chemical analyses also indicate that the Ca-birnessite phases produced at lower pH values are distinct from those generated by a 1 Ca^{2+} for 2 Na^+ exchange at higher pH. For Ca-birnessites formed at pH 3 using 0.1 and 0.01 *M* Ca^{2+}, the measured Ca/Mn ratios were only ~0.07 rather than ~0.16, and the Ca/Mn values for all of the samples exchanged at pH 2 ranged between 0.03 and 0.06. The smaller number for interlayer Ca^{2+} is consistent with a hexagonal birnessite structure in which the negative charge on the octahedral sheet is balanced by higher concentrations of interlayer Mn^{2+}.

Indeed, our Rietveld refinement for the sample exchanged with 0.01 *M* Ca^{2+} at pH 2 yielded a nominally triclinic unit-cell that was very close to that expected for a hexagonal structure; the value for α was 91.8°, instead of the expected 90°. When the refinement was performed using space group *P*-3, the goodness-of-fit values did not differ significantly from those using the *C*-1 triclinic cell. The atomic parameters determined with S.G. *P*-3 were nearly identical to those of hexagonal H-birnessite, including the refined Mn occupancy of ~0.90. This occupancy is significantly lower than those refined for the triclinic Ca-birnessite structures at higher pH (Mn_{occ} ~0.94). For the exchanges at pH 2, the XPS results (Table 2) indicate the reduction of Mn^{3+} to Mn^{2+}, resulting in octahedral vacancies as Mn^{2+} migrated into the interlayer (Lanson et al. 2000). Difference Fourier maps of these Ca-birnessites exchanged at very low pH revealed electron densities above and below the octahedral sites, consistent with interlayer Mn^{2+} (and possibly some Ca^{2+} and Mn^{3+}) in tridentate coordination with vacant octahedral sites. The loss of the larger Mn^{3+}, relative to Mn^{4+}, from the octahedral sheets also is consistent with the change in the average Mn-O distances determined from the Rietveld refinements, which are ~1.95 Å for the triclinic Ca-birnessite structures, but only ~1.92 Å for the hexagonal Ca-birnessite.

Mechanism of Ca-induced reduction of Mn^{3+}. Although it is well-established that dissolved transition metals will reduce $Mn^{3+/4+}$ in birnessite to Mn^{2+} through direct electron transfer from the transition metal (Feng et al. 2004, 2007; Fischer 2010; Fischel et al. 2015), the mechanism by which the exchange of Na^+ by Ca^{2+} causes reduction of Mn^{3+} cannot involve the oxidation of Ca^{2+}. The Ca-O interaction would further lengthen and destabilize the Mn^{3+}-O bond, favoring a disproportionation reaction as described by Silvester et al. (1997): $2Mn^{3+} \rightarrow Mn^{2+} + Mn^{4+}$. The Mn^{2+} cation is sterically too large for the octahedral sheet and relocates either to a tridentate position above the resulting octahedral vacancy, inducing at least some of the Ca to relocate to the $z \sim 0.5$ plane, or else the Mn^{2+} is lost to solution. As a result of the decrease in octahedral strain, the triclinic distortion in Ca-birnessite is markedly lower than is observed in Na-, K-, Ba-, or Cs-birnessites (Lopano et al. 2007, 2009).

When pH is very low, the Ca^{2+} cations must compete with H^+ cations for those Jahn-Teller distorted O anions. Thus, in our experiments, the transition from triclinic to hexagonal structures occurred for all exchanges at pH 2 (H^+ concentration = 0.01 *M*), and for sufficiently low concentrations of Ca^{2+} (0.1 and 0.01 *M* Ca^{2+}) at pH 3 (H^+ concentration = 0.001 *M*). Tellingly, when the Ca^{2+} concentration was 1.0 *M* at pH 3, the full 1:2 Ca-for-Na exchange occurred, and the final structure was triclinic. Thus, at certain H/Ca values the smaller and more mobile H^+ cations gain a competitive advantage, and a tipping point occurs when Ca concentrations fall between 0.1 and 1.0 M Ca^{2+} at pH 3.

Superstructures

SAED patterns of the Ca-birnessites exchanged at pH 7.5 typically showed faint superstructure reflections at 1/3 [200]* (Fig. 9B). Drits et al. (1998) also report superstructure reflections in SAED patterns for their synthetic Ca-birnessite, but different from those we observed. In one variant, $a_{super} = 3a$, $b_{super} = 3b$, and $c_{super} = 4c$. Another variant represents an interstratification of two cells with $a_{super} = 3/2\ (a - b)$, $b_{super} = 4b$, and $c = 4c$ alternating with $a_{super} = 3/2(a + b)$, $b_{super} = -4b$, and $c_{super} = 4c$. The disparity in superperiodicities that we observed relative to the complex superstructures reported by Drits et al. (1998) may be explained by differences in the preparation of the Ca-birnessite samples. Whereas our samples were produced by simple exchange of Na-birnessite in neutral $CaCl_2$ solutions, Drits et al. (1998) exchanged Na-buserite in $Ca(NO_3)_2$ solutions without controlling pH, which typically attained values of 9 to 10 in their experiments.

By contrast, Ca-birnessite samples generated from the reaction of triclinic Na-birnessite at pH 2 with either 0.1 or 1 *M* $CaCl_2$ produced selected area electron diffraction patterns that typically were free of streaks or superstructure reflections (Fig. 8B). HRTEM images of these crystals (Fig. 8C) likewise showed few microstructural defects, although faint superstructure reflections halfway along the [100]* and [010]* directions were sometimes apparent, suggesting doubling of *a* and *b* in local areas.

We suggest that the superstructure reflections arise from short-range order among the interlayer Ca atoms and water molecules. This assumption is supported by the observation that different interlayer cations result in different patterns of superstructure reflections (Post and Veblen 1990; Drits et al. 1997, 1998; Lopano et al. 2007, 2009). In contrast, hexagonal birnessite structures show faint or no superstructure reflections because most of the interlayer cations are locked into sites above and below octahedral vacancies. Drits et al. (1997) postulate that the superstructures indicate ordering of distorted Mn^{3+} octahedra into rows, such that one row of Mn^{3+} octahedra alternate with two rows of Mn^{4+} octahedra. However, we observed no direct evidence of such ordering, and the energetics of structural strain suggest to us that Mn^{3+} cations will tend not to occupy neighboring octahedra, similar to the distribution of Al^{3+} in silicates described by the Al-avoidance rule (Loewenstein 1954; Post and Burnham 1986). In other words, the energy minimization realized by isolating Mn^{3+} is greater than might be obtained by any strain reduction achieved by aligning Jahn-Teller distortions in rows. Additionally, XRD structure refinements reported for large tunnel structure Mn oxides, such as romanechite, todorokite, and woodruffite (Turner and Post 1988; Post et al. 2003) consistently show that Mn^{3+} preferentially orders into octahedra that are at the edges of the widest octahedral chains (*e.g.*, triple chains, or quadruple chains). But in all cases, charge balance considerations and refined Mn octahedral bond distances show that less than half of the octahedra in any particular chain are occupied by Mn^{3+}, thereby avoiding nearest neighbor Mn^{3+} octahedra (as would be the case in the proposed rows of octahedra). Finally, when considering the total structure energy, one must also consider contributions resulting from interlayer cation charge-charge interactions with the Mn in the octahedral sheets. Although a possible secondary effect, previous structure-energy studies indicate a tendency for the interlayer cations to align with the Mn^{3+} octahedra, producing a three-dimensional configuration with Mn^{3+} and interlayer cations occupying approximately 1/3 of the available sites (Cygan et al. 2012).

Drits et al. (1998) concluded that their Ca-birnessite samples were composed of mixtures of various structures consistent with the SAED superstructure reflections, and, in fact, such a model might be correct. The *C*-1 structure model presented in the current study likely represents the long-range average structure, as does X-ray diffraction data, and yields excellent overall Rietveld refinements for triclinic Ca-birnessite samples exchanged over a range of pH values and Ca concentrations.

Comparison of synthetic Ca-birnessite and ranciéite

Ca-rich birnessite-like phases are common in a variety of natural systems (*e.g.*, Tebo et al. 2004; Bargar et al. 2005; Webb et al. 2005; Tan et al. 2010). In most of these cases, it was assumed, or at least suggested, that the Mn oxide phases formed by some type of biologically mediated process involving bacteria, fungi, or similar microorganisms. Additionally, the Ca-analogue to the mineral birnessite, ranciéite, has been found as an abiogenic product in numerous low-temperature alpine vein deposits and in oxidized zones of Fe and Mn deposits (Ertl et al. 2005). Apparently, Ca cations either are particularly effective at stabilizing birnessite-like structures, or Ca-rich birnessites are energetically or kinetically favored in natural environments. Furthermore, as mentioned above, ranciéite-like structures play critical roles in water-oxidation catalysis and as the oxygen-evolving complex within the enzyme photosystem II (PSII) (Umena et al. 2011; Zhang et al. 2015; Yamaguchi et al. 2017).

Ranciéite ($Ca_{0.19}K_{0.01}(Mn^{4+}_{0.91}\square_{0.09})O_2 \cdot 0.63\ H_2O$) has a hexagonal structure (Post et al. 2008) that is similar to those of the Ca-birnessites generated when we exchanged Na-birnessite at low pH and low Ca concentrations. In ranciéite, 9% of the octahedra are vacant, in comparison with the 10% vacancy content of the exchanged Ca-birnessite synthesized at pH 2 and 0.01 *M* Ca^{2+} in this study. The Ca:Mn ratio in ranciéite is 0.21, significantly higher than the average values of ~0.05 observed for the hexagonal Ca-birnessites here (Fig. 3). This disparity is explained by the fact that the ranciéite formed in alpine vein deposits revealed no evidence for Mn^{2+}, which we surmise occurs as an interlayer cation in our exchanged Ca-birnessites.

In both ranciéite and hexagonal Ca-birnessite produced by exchange, Ca cations occupy positions above and below vacancies in the Mn octahedral sheets. Further, through tridentate coordination with the octahedral O atoms associated with the vacancies and tridentate coordination with water molecules at $z = 0.5$, the Ca^{2+} (and/or Mn^{2+}) cations occupy highly regular octahedral sites within the interlayer (Fig. 1C). Fischer et al. (2018) have argued that the presence of these cations is at least as important as the absence of distortional Mn^{3+} in promoting the *P*-3 symmetry of hexagonal birnessite structures, since selective removal of octahedral Mn^{3+} from triclinic birnessite by siderophores induced no symmetry change.

Although the Ca-exchanged birnessite structures exchanged above pH 3 were unambiguously triclinic, this study does reinforce the conclusion in Ling et al. (2018) that Ca-birnessites are "less triclinic" – with smaller distortions from hexagonal symmetry – than are Na-, K-, Ba-, and Cs-birnessite. In addition, when the percentages of Mn^{2+} and Mn^{3+} as measured by XPS are compared for different varieties of birnessite, the triclinic birnessites cluster separately from the synthetic and natural hexagonal birnessites (Fig. 10). Moreover, the Ca-birnessites from the present study reside close to the morphotropic phase boundaries (Heaney 2000) that separate the triclinic and hexagonal symmetry fields. Thus, triclinic Ca-birnessite is in a sense transitional between hexagonal ranciéite-type birnessites and the other triclinic alkali- and alkaline-earth birnessites. Moreover, in the triclinic Ca-birnessite phases, our refinements indicate that at least some of the Ca^{2+} is disordered with water molecules halfway between the octahedral sheets. Perhaps then, the size and charge of Ca^{2+} confers a flexibility to occupy different interlayer sites equally well, making it a particularly effective partner with Mn to build birnessite- (or ranciéite-) like structures. Moreover, to the extent that Ca^{2+} is equally capable of coordinating with octahedral O atoms alongside Mn^{2+} at $z = 0.7$ or coordinating with water molecules near $z = 0.5$, these results may offer some insights into the mechanism of the $CaMn_4$ oxygen-evolving complex, particularly since Mn redox changes are associated with these different interlayer positions.

IMPLICATIONS

Ca-rich phyllomanganates occur in a variety of natural systems, and detailed knowledge of their structures is essential to understanding, and modeling, their roles as geochemical agents. The exchange experiments described here, performed over a range of pH values (3 to 7.5) and Ca^{2+} concentrations (0.01 to 1 M) that are relevant to natural environments, yielded Ca-birnessite products that all have the same triclinic structure with nearly identical unit-cell parameters. This observation suggests the existence of a Ca-birnessite structure that is distinct from that of other triclinic birnessite phases with different interlayer cations. Our results also reveal that the transformation of Na- to Ca-birnessite is more than a simple replacement of Na by Ca; in addition to adjustments to the layer stacking configuration to accommodate a different size/charge cation, as evidenced by the changes in unit-cell angles, some of the Mn^{3+} cations in the octahedral layers are reduced to Mn^{2+}, which migrates into the interlayer. As various studies have suggested that Mn^{3+}, and vacancies, in the octahedral sheets are particularly active sites for cation absorption and/or redox reactions, our work indicates that the identities of interlayer cations affect the Mn oxidation profile and consequently the reactivity of phyllomanganates. Additionally, the XPS results show that although the relative amounts of the different Mn oxidation states change for the various Ca-exchanges, the average oxidation states remain the same, indicating that although there is a transfer of electrons within a particular birnessite phase, there is not net change in the overall redox state.

Samples produced by Ca-exchange at pH values of 2 and 3 have significantly lower Ca contents than those formed under higher pH conditions, and exhibit hexagonal, or nearly hexagonal, structures, or are mixtures of hexagonal and triclinic phases. The hexagonal structure compares closely with those previously reported for synthetic hexagonal birnessite-like phases and for the mineral ranciéite. We propose that the structures determined here for triclinic Ca-birnessite and hexagonal Ca-birnessite are improved analogues for modeling natural Ca-phyllomanganates. Additionally, the charge and size characteristics of Ca^{2+} perhaps make it particularly suited for forming birnessite/ranciéite-like structures, *e.g.* the oxygen-evolving complex within the enzyme photosystem II (PSII).

ACKNOWLEDGMENTS

This research was carried out at National Museum of Natural History, Department of Mineral Sciences, Smithsonian Institution. Scott D. Whittaker is kindly acknowledged for his technical support during the use of FEI Apreo scanning electron microscope at National Museum of Natural History, Smithsonian Institution. Si Athena Chen collected synchrotron X-ray diffraction data at Beamline 13-BM_C at the Advanced Photon Source, Argonne National Laboratory. Ke Wang assisted with transmission electron microscopy in the Materials Characterization Laboratory, Penn State. We also acknowledge NSF EAR-1552211 and the Miller Faculty Fellowship (College of Earth and Mineral Sciences, PSU). This research used resources of the Advanced Photon Source, a U.S. Department of Energy (DOE) Office of Science User Facility operated for the DOE Office of Science by Argonne National Laboratory under Contract No. DE-AC02-06CH11357. ESI was supported by U.S. Department of Energy (DOE), Office of Science, Office of Basic Energy Sciences (BES), Chemical Sciences, Geosciences, and Biosciences Division through its Geosciences program at Pacific Northwest National Laboratory (PNNL). PNNL is a multiprogram national laboratory operated by Battelle Memorial Institute under Contract No. DE-AC05-76RL01830 for the U.S. DOE. A portion of the research was performed using EMSL (grid.436923.9), a DOE Office of Science User Facility sponsored by the Office of Biological and Environmental Research. Four anonymous reviewers are kindly acknowledged for their thoughtful comments and suggestions that significantly improved the manuscript.

REFERENCES

Adreiadis, E.S., Chavarot-Kerlidou, M., Fontecave, M., and Artero, V. (2011) Artificial photosynthesis: from molecular catalysts for light-driven water splitting to photoelectrochemical cells. Photochemistry and Photobiology, 87(5), 946-64.

Bargar, J.R., Fuller, C.C., Marcus, M.A., Brearley, A.J., De la Rosa, M.P., Webb, S.M. and Caldwell, W.A. (2009). Structural characterization of terrestrial microbial Mn oxides from Pinal Creek, AZ. Geochimica et Cosmochimica Acta, 73, 889-910.

Boumaiza, H., Renard, A., Robinson, M.R., Kervern, G., Vidal, L., Ruby, C., Bergaoui, L., and Coustel, R. (2019) A multi-technique approach for studying Na triclinic and hexagonal birnessites. Journal of Solid State Chemistry, 272, 234-243.

Chukhrov, F.V., Gorshkov, A.I., Sivtsov, A.V., and Berezovskaya, V.V. (1979) A new 14 Å mineral of the birnessite group in deep-sea micronodules. Nature, 280, 136-137.

Cui, H., Liu, F., Feng, X., Tan, W., and Wang, M.K. (2010) Aging promotes todorokite formation from layered manganese oxide at near-surface conditions. Journal of Soils and Sediments, 10(8), 1540-1547.

Cygan, R.T., Post, J.E., Heaney, P.J. and Kubicki, J.D. (2012) Molecular models of brinessite and related hydrated layered minerals. American Mineralogist, 97, 1505-1514.

Drits, V.A., Lanson, B., Gorshkov, A.I., and Manceau, A. (1998) Substructure and superstructure of four-layer Ca-exchanged birnessite. American Mineralogist, 83(1-2), 97-118.

Drits, V.A., Silvester, E., Gorshkov, A.I., and Manceau, A. (1997) Structure of synthetic monoclinic Na-rich birnessite and hexagonal birnessite: I. Results from X-ray diffraction and selected-area electron diffraction. American Mineralogist, 82, 946–961.

Ertl, A., Pertlik, F., Prem, M., Post, J.E., Kim, S.J., Brandstatter, F., and Schuster, R. (2005) Ranciéite crystals from Friesach, Carinthia, Austria. European Journal of Mineralogy, 17, 163–172.

Feng, M., Du, Q., Su, L., Zhang, G., Wang, G., Ma, Z., Gao, W., Qin, X., and Shao, G. (2017) Manganese oxide electrode with excellent electrochemical performance for sodium ion batteries by pre-intercalation of K and Na ions. Nature Scientific Reports, 7(1), 2219.

Feng, X.H., Liu, F., Tan, W.F., and Liu, X.W. (2004) Synthesis of Birnessite from the Oxidation of Mn^{2+} by O_2 in Alkali Medium: Effects of Synthesis Conditions. Clays and Clay Minerals, 52(2), 240-250.

Feng, X.H., Zhai, L.M., Tan, W.F., Liu, F., and He, J.Z. (2007) Adsorption and redox reactions of heavy metals on synthesized Mn oxide minerals. Environmental Pollution 147(2), 366-73.

Finger, L.W., Cox, D.E., and Jephcoat, A.P. (1994) A correction for powder diffraction peak asymmetry due to axial divergence. Journal of Applied Crystallography, 27(6), 892-900.

Fischel, M.H., Fischel, J.S., Lafferty, B.J., and Sparks, D.L. (2015) The influence of environmental conditions on kinetics of arsenite oxidation by manganese-oxides. Geochemical Transactions, 16, 15.

Fischer, T.B. (2010) Structural Transformations of Birnessite (δ-MnO_2) During Biological and Abiological Reduction. Doctoral dissertation, Pennsylvania State University.

Fischer, T.B., Heaney, P.J. and Post, J.E. (2018). Changes in the structure of birnessite during siderophore-promoted dissolution: A time-resolved synchrotron X-ray diffraction study. Chemical Geology, 476, 46-58.

Fleeger, C.R., Heaney, P.J., and Post, J.E. (2013) A time-resolved X-ray diffraction study of Cs exchange into hexagonal H-birnessite. American Mineralogist, 98, 671-679.

Frey, C.E., Wiechen, M., and Kurz, P. (2014) Water-oxidation catalysis by synthetic manganese oxides--systematic variations of the calcium birnessite theme. Dalton Transactions, 43(11), 4370-9.

Golden, D.C., Dixon, J.B., and Chen, C.C. (1986) Ion exchange, thermal trasformations, and oxidizing properties of birnessite. Clays and Clay Minerals, 34(5), 511-520.

Grangeon, S., Lanson, B., Miyata, N., Tani, Y. and Manceau, A. (2010). Structure of nanocrystalline phyllomanganates produced by freshwater fungi. American Mineralogist, 95, 1608-1616.

Händel, M., Rennert, T., and Totsche, K.U. (2013) A simple method to synthesize birnessite at ambient pressure and temperature. Geoderma, 193-194, 117-121.

Heaney, P.J. (2000). Phase transformations induced by solid solution. Reviews in Mineralogy and Geochemistry, 39, 135-174.

Hinkle, M.A.G., Flynn, E.D., and Catalano, J.G. (2016) Structural response of phyllomanganates to wet aging and aqueous Mn(II). Geochimica Et Cosmochimica Acta, 192, 220-234.

Hou, H.J.M. (2011) Manganese-based Materials Inspired by Photosynthesis for Water-Splitting. Materials 4(10), 1693-1704.

Housecroft, C.E., and Jenkins, H.D.B. (2017) Absolute ion hydration enthalpies and the role of volume within hydration thermodynamics. Rsc Advances, 7(45), 27881-27894.

Hsu, Y. K., Chen, Y. C., Lin, Y. G., Chen, L. C., & Chen, K. H. (2011). Reversible phase transformation of MnO_2 nanosheets in an electrochemical capacitor investigated by in situ Raman spectroscopy. Chemical Communications, 47, 1252-1254.

Huang, M., Zhang, Y., Li, F., Zhang, L., Ruoff, R.S., Wen, Z., and Liu, Q. (2014) Self-assembly of mesoporous nanotubes assembled from interwoven ultrathin birnessite-type MnO_2 nanosheets for asymmetric supercapacitors. Nature Scientific Reports, 4, 3878.

Ilton, E.S., Post, J.E., Heaney, P.J., Ling, F.T. and Kerisit, S.N. (2016) XPS determination of Mn oxidation states in Mn (hydr) oxides. Applied Surface Science, 366, 475-485.

Iyer, A., Del-Pilar, J., King'ondu, C.K., Kissel, E., Garces, H.F., Huang, H., El-Sawy, A.M., Dutta, P.K., and Suib, S.L. (2012) Water Oxidation Catalysis using Amorphous Manganese Oxides, Octahedral Molecular Sieves (OMS-2), and Octahedral Layered (OL-1) Manganese Oxide Structures. Journal of Physical Chemistry C, 116(10), 6474-6483.

Jiao, F., and Frei, H. (2010) Nanostructured manganese oxide clusters supported on mesoporous silica as efficient oxygen-evolving catalysts. Chemical Communications, 46(17), 2920-2.

Johnson, E.A., and Post, J.E. (2006) Water in the interlayer region of birnessite: Importance in cation exchange and structural stability. American Mineralogist, 91(4), 609-618.

Jones, L.H.P., and Milne, A.A. (1956) Birnessite, a new manganese oxide mineral from Aberdeenshire, Scotland. Mineralogical Magazine, 31, 283-288.

Julien, C. (2003) Raman spectra of birnessite manganese dioxides. Solid State Ionics, 159(3-4), 345-356.

Julien, C.M., Massot, M., and Poinsignon, C. (2004) Lattice vibrations of manganese oxides. Spectrochimica Acta Part A: Molecular and Biomolecular Spectroscopy, 60(3), 689-700.

Kim, S.J. (1980) Birnessite and ranciete problem; their crystal chemistry and new classification. Journal of the Geological Society of Korea, 16, 105–113.

Kim, S.J. (1991) New characterization of takanelite. American Mineralogist, 76, 1426-1430.

Kong, Kyeong Pil (2017) Mineralogical and geochemical constraints of chromium oxidation induced by birnessite. Master's Thesis, Pennsylvania State University.

Kuma, K., Usui, A., Paplawsky, W., Gedulin, B., and Arrhenius, G. (1994) Crystal Structures of Synthetic 7 Å and 10 Å Manganates Substituted by Mono- and Divalent Cations. Mineralogical Magazine, 58, 425-447.

Kwon, K.D., Refson, K., and Sposito, G. (2013) Understanding the trends in transition metal sorption by vacancy sites in birnessite. Geochimica Et Cosmochimica Acta, 101, 222-232.

Landrot, G., Ginder-Vogel, M., Livi, K., Fitts, J.P., and Sparks, D.L. (2012) Chromium(III) oxidation by three poorly crystalline manganese(IV) oxides. 2. Solid phase analyses. Environmental Science &Technology, 46(21), 11601-9.

Lanson, B., Drits, V.A., Silvester, E., and Manceau, A. (2000) Structure of H-exchanged hexagonal birnessite and its mechanism of formation from Na-rich monoclinic buserite at low pH. American Mineralogist, 85, 826–838.

Le Goff, P., Baffier, N., Bach, S., and Pereira-Ramos, J.P. (1996) Synthesis, ion exchange and electrochemical properties of lamellar phyllomanganates of the birnessite group. Materials Research Bulletin, 31(1), 63-75.

Leinenweber, K. (2005) Welcome to the Crystal Cracker program page, by Kurt Leinenweber. http://multianvil.asu.edu/Crystal_Cracker/CrystalCracker.html (accessed March 19, 2019)

Lefkowitz, J.P., Rouff, A.A., and Elzinga, E.J. (2013) Influence of pH on the reductive transformation of birnessite by aqueous Mn(II). Environmental Science & Technology, 47(18), 10364-71.

Ling, F.T., Heaney, P.J., Post, J.E., and Gao, X. (2015) Transformations from triclinic to hexagonal birnessite at circumneutral pH induced through pH control by common biological buffers. Chemical Geology, 416, 1-10.

Ling, F.T., Post, J.E., Heaney, P.J., and Ilton, E.S. (2018) The relationship between Mn oxidation state and structure in triclinic and hexagonal birnessites. Chemical Geology, 479, 216-227.

Ling, F.T., Post, J.E., Heaney, P.J., Kubicki, J.D., and Santelli, C.M. (2017) Fourier-transform infrared spectroscopy (FTIR) analysis of triclinic and hexagonal birnessites. Spectrochimica Acta Part A:Molecular and Biomolecular Spectroscopy, 178, 32-46.

Loewenstein, W. (1954) The distribution of aluminum in the tetrahedra of silicates and aluminates. American Mineralogist, 39, 92-96.

Lopano, C.L., Heaney, P.J., Post, J.E., Hanson, J., and Komarneni, S. (2007) Time-resolved structural analysis of K- and Ba-exchange reactions with synthetic Na-birnessite using synchrotron X-ray diffraction. American Mineralogist, 92(2-3), 380-387.

Lopano, C.L., Heaney, P.J., Bandstra, J.Z., Post, J.E., and Brantley, S.L. (2011) Kinetic analysis of cation exchange in birnessite using time-resolved synchrotron X-ray diffraction. Geochimica et Cosmochimica Acta, 75, 3973-3981.

Lopano, C.L., Heaney, P.J. and Post, J.E. (2009) Cs-exchange in birnessite: Reaction mechanisms inferred from time-resolved X-ray diffraction and transmission electron microscopy. American Mineralogist, 94, 816-826.

Manceau, A., Lanson, B., and Drits, V.A. (2002) Structure of heavy metal sorbed birnessite. Part III: Results from powder and polarized extended X-ray absorption fine structure spectroscopy. Geochimica Et Cosmochimica Acta, 66(15), 2639-2663.

Manning, B.A., Fendorf, S.E., Bostick, B., and Suarez, D.L. (2002) Arsenic(III) oxidation and arsenic(V) adsorption reactions on synthetic birnessite. Environmental Science & Technology, 36(5), 976-81.

McKenzie, R.M. (1971) The Synthesis of Birnessite, Cryptomelane, and Some Other Oxides and Hydroxides of Manganese. Mineralogical Magazine, 38(296), 493-502.

McKeown, D.A., and Post, J.E. (2001) Characterization of manganese oxide mineralogy in rock varnish and dendrites using X-ray absorption spectroscopy. American Mineralogist, 86, 701-713.

Najafpour, M.M., Salimi, S., Madadkhani, S., Holynska, M., Tomo, T., and Allakhverdiev, S.I. (2016) Nanostructured manganese oxide on silica aerogel: a new catalyst toward water oxidation. Photosynthesis Research, 130(1-3), 225-235.

Najafpour, M.M., Sedigh, D.J., Pashaei, B., and Nayeri, S. (2013) Water oxidation by nano-layered manganese oxides in the presence of cerium(IV) ammonium nitrate: important factors and a proposed self-repair mechanism. New Journal of Chemistry, 37(8), 2448-2459.

Nambu, M. and Tanida, K. (1971) New mineral takanelite. The Journal of the Japanese Association of Mineralogists, Petrologists and Economic Geologists, 65, 1-5.

Post, J.E. (1999) Manganese oxide minerals: crystal structures and economic and environmental significance. Proceedings of the National Academy of Sciences of the United States of America, 96(7), 3447-54.

Post, J.E. and Burnham, C.W. (1986) Ionic modeling of mineral structures and energies in the electron gas approximation: TiO_2 polymorphs, quartz, forsterite, diopside. American Mineralogist, 71, 142-150.

Post, J.E., Heaney, P.J., Cahill, C.L., and Finger, L.W. (2003) Woodruffite: A new Mn oxide structure with 3 x 4 tunnels. American Mineralogist, 88, 1697-1702.

Post, J.E., Heaney, P.J., and Ertl, A. (2008) Rietveld refinement of the rancíéite structure using synchrotron powder diffraction data. Powder Diffraction, 23(01), 10-14.

Post, J.E., Heaney, P.J., and Hanson, J. (2002) Rietveld refinement of a triclinic structure for synthetic Na-birnessite using synchrotron powder diffraction data. Powder Diffraction, 17(3), 218-221.

Post, J.E., Heaney, P.J., and Hanson, J. (2003) Synchrotron X-ray diffraction study of the structure and dehydration behavior of todorokite. American Mineralogist, 88, 142-150.

Post, J.E., and Veblen, D.R. (1990) Crystal structure determinations of synthetic sodium, magnesium, and potassium birnessite using TEM and the Rietveld method. American Mineralogist, 75, 477-489.

Prescher, C. and Prakapenka, V.B. (2015) DIOPTAS: A program for reduction of two-dimensional X-ray diffraction data and data exploration. High Pressure Research, 35, 223–230.

Rietveld, H.M. (1969) A Profile Refinement Method for Nuclear and Magnetic Structures. Journal of Applied Crystallography, 2(2), 65-71.

Santelli, C.M., Webb, S.M., Dohnalkova, A.C. and Hansel, C.M. (2011). Diversity of Mn oxides produced by Mn (II)-oxidizing fungi. Geochimica et Cosmochimica Acta, 75, 2762-2776.

Sauer, K., and Yachandra, V.K. (2002) A possible evolutionary origin for the Mn4 cluster of the photosynthetic water oxidation complex from natural MnO_2 precipitates in the early ocean. Proceedings of the National Academy of Sciences, 99(13), 8631-6.

Shannon, R.D. (1976) Revised Effective Ionic Radii and Systematic Studies of Interatomie Distances in Halides and Chaleogenides. Acta crystallographica. Section A, Foundations of crystallography 32, 751-767.

Shannon, R.D., Gumerman, P.S., and Chenavas, J. (1975) Effect of octahedral Distortion on Mean Mn^{3+}-O Distance. American Mineralogist, 60, 714-716.

Shumlas, S.L., Singireddy, S., Thenuwara, A.C., Attanayake, N.H., Reeder, R.J., and Strongin, D.R. (2016) Oxidation of arsenite to arsenate on birnessite in the presence of light. Geochemical Transactions, 17, 5.

Silvester, E., Manceau, A., and Drits, V.A. (1997) Structure of synthetic monoclinic Na-rich birnessite and hexagonal birnessite: II. Results from chemical studies and EXAFS spectroscopy. American Mineralogist, 82, 962-978.

Smith, D.W. (1977) Ionic Hydration Enthalpies. Journal of Chemical Education, 54(9), 540-542.

Stephens, P. (1999) Phenomenological model of anisotropic peak broadening in powder diffraction. Journal of Applied Crystallography, 32(2), 281-289.

Tan, H., Zhang, G.X., Heaney, P.J., Webb, S.M., and Burgos, W.D. (2010) Characterization of manganese oxide precipitates from Appalachian coal mine drainage treatment systems. Applied Geochemistry, 25(3), 389-399.

Tan, W.F., Lu, S.J., Liu, F., Feng, X.H., He, J.Z., and Koopall, L.K. (2008) Determination of the point-of-zero, charge of manganese oxides with different methods including an improved salt titration method. Soil Science, 173(4), 277-286.

Tebo, B.M., Bargar, J.R., Clement, B.G., Dick, G.J., Murray, K.J., Parker, D., Verity, R., and Webb, S. M. (2004). Biogenic manganese oxides: properties and mechanisms of formation. Annual Reviews in Earth and Planetary Science, 32, 287-328.

Thompson, P., Cox, D.E., and Hastings, J.B. (1987) Rietveld refinement of Debye-Scherrer synchrotron X-ray data from Al2O3. Journal of Applied Crystallography, 20(2), 79-83.

Toby, B.H., and Von Dreele, R.B. (2013) GSAS-II: the genesis of a modern open-source all purpose crystallography software package. Journal of Applied Crystallography, 46(2), 544-549.

Tu, S., Racz, G.J., and Goh, T.B. (1994) Transformations of Synthetic Birnessite as Affected by pH and Manganese Concentration. Clays and Clay Minerals, 42(3), 321-330.

Turner, S. and Post, J.E. (1988) Refinement of the substructure and superstructure of romanechite. American Mineralogist, 73, 1155-1161

Umena, Y., Kawakami, K., Shen, J. R. and Kamiya, N. (2011). Crystal structure of oxygen-evolving photosystem II at a resolution of 1.9 Å. Nature, 473, 55-60.

Wang, M.X., Wang, Y.P., Tan, W.F., Liu, F., Feng, X.H., and Koopal, L.K. (2010) Effect of 1-1 electrolyte concentration on the adsorption/desorption of copper ion on synthetic birnessite. Journal of Soils and Sediments, 10(5), 879-885.

Wang, Y., Feng, X.H., Villalobos, M., Tan, W.F., and Liu, F. (2012) Sorption behavior of heavy metals on birnessite: Relationship with its Mn average oxidation state and implications for types of sorption sites. Chemical Geology, 292, 25-34.

Webb, S.M., Tebo, B.M. and Bargar, J.R. (2005). Structural characterization of biogenic Mn oxides produced in seawater by the marine Bacillus sp. strain SG-1. American Mineralogist, 90, 1342-1357.

Wiechen, M., Zaharieva, I., Dau, H., and Kurz, P. (2012) Layered manganese oxides for water-oxidation: alkaline earth cations influence catalytic activity in a photosystem II-like fashion. Chemical Science, 3(7), 2330-2339.

Wiechen, M., Najafpour, M.M., Allakhverdiev, S.I. and Spiccia, L. (2014) Water oxidation catalysis by manganese oxides: learning from evolution. Energy & Environmental Science, 7, 2203-2212.

Witzke, T., Pöllmann, H., Gardolinski, J.E.F.C. and Sommariva,M. (2017) Lagalyite, IMA 2016, 106.

Yamaguchi, K., Shoji, M., Isobe, H., Yamanaka, S., Umena, Y., Kawakami, K. and Kamiya, N. (2017) On the guiding principles for understanding of geometrical structures of the CaMn4O5 cluster in oxygen-evolving complex of photosystem II. Proposal of estimation formula of structural deformations via the Jahn–Teller effects. Molecular Physics, 115, 636-666.

Yang, L.F., Cheng, S., Ji, X., Jiang, Y., Zhou, J., and Liu, M.L. (2015) Investigations into the origin of pseudocapacitive behavior of Mn_3O_4 electrodes using in operando Raman spectroscopy. Journal of Materials Chemistry A, 3(14), 7338-7344.

Yin, H., Liu, F., Feng, X., Hu, T., Zheng, L., Qiu, G., Koopal, L.K., and Tan, W. (2013) Effects of Fe doping on the structures and properties of hexagonal birnessites – Comparison with Co and Ni doping. Geochimica et Cosmochimica Acta, 117, 1-15.

Zaharieva, I., Gonzalez-Flores, D., Asfari, B., Pasquini, C., Mohammadi, M.R., Klingan, K., Zizak, I., Loos, S., Chernev, P. and Dau, H. (2016). Water oxidation catalysis–role of redox and structural dynamics in biological photosynthesis and inorganic manganese oxides. Energy & Environmental Science, 9, 2433-2443.

Zhang, C., Chen, C., Dong, H., Shen, J. R., Dau, H. and Zhao, J. (2015) A synthetic Mn4Ca-cluster mimicking the oxygen-evolving center of photosynthesis. Science, 348, 690-693.

Zhao, H., Zhu, M., Li, W., Elzinga, E.J., Villalobos, M., Liu, F., Zhang, J., Feng, X., and Sparks, D.L. (2016) Redox Reactions between Mn(II) and Hexagonal Birnessite Change Its Layer Symmetry. Environmental Science & Technology, 50(4), 1750-8.

FIGURE CAPTIONS

Figure 1. Structure drawings showing a) triclinic Na-birnessite, b) triclinic Ca-birnessite – pH 7.5 and 1 *M* Ca^{2+}, and c) hexagonal Ca-exchanged birnessite – pH 2 and 0.01 *M* Ca^{2+}. Magenta atoms - Mn; red atoms - O; yellow atoms – Na/H_2O; purple atoms – Ca/H_2O; blue atoms – Mn^{2+}/Ca^{2+}.

Figure 2. Scanning Electron microscopy (SEM) image of Ca-birnessite.

Figure 3. Graph reporting Ca/Mn ratio in Ca-birnessite structures prepared at different conditions of pH and Ca^{2+} concentration. Asterisk = Ca birn 1M (5min); Green diamond = Ca birn 1M; blue triangle = Ca birn 0.1M; yellow circle= Ca birn 0.1M+DI water; red square = Ca birn 0.01M.

Figure 4. X-ray diffraction (XRD) patterns for Ca-birnessite samples exchanged with 1 M $CaCl_2 \cdot 2H_2O$ solutions.

Figure 5. Rietveld refinement fits and difference curve for a) triclinic Ca-birnessite exchanged at pH 7.5 and 0.1M Ca^{2+}, and b) hexagonal birnessite exchanged at pH 2 and 0.01M Ca^{2+}. Observed pattern: blue crosses, calculated pattern: solid green line, and difference between the observed and calculated patterns pattern: aquamarine line.

Figure 6. Fourier transform infrared spectroscopy (FT-IR) spectra collected in the Mn-O bond vibration range for Ca-birnessite prepared with $CaCl_2 \cdot 2H_2O$ solutions (a) initially at near-neutral pH; (b) initially at pH 3; (c) initially at pH 2.

Figure 7. Raman spectra of Ca-birnessite synthesized in this study.

Figure 8. (A) Bright-field TEM image of Ca-birnessite exchanged using 0.1 *M* $CaCl_2$ solution at pH 2. (B) Selected area electron diffraction pattern along [001] shows no streaking or

superstructures, consistent with space group $P\bar{3}$. C) A high-resolution image of Ca-birnessite (ZA [001]) exchanged at pH 2 with 0.1 *M* $CaCl_2$ solution with fast-Fourier transform (FFT, inset). Very weak superperiodic reflections are evident halfway along [100]* and [010]*.

Figure 9. (A) Bright-field TEM image of a crystal formed from Na-birnessite exchanged with 0.1 *M* $CaCl_2$ solution at pH 7.5. Dark and light surface striations are typical of these crystals, with a ~59º angle between striations. (B) SAED patterns were best indexed to triclinic C $\bar{1}$. cell, and superperiodic reflections at 1/3 [200]* were apparent. C) An HRTEM image of Ca-birnessite synthesized from triclinic Na-birnessite at pH 7.5 and 0.1 *M* $CaCl_2$ solution with FFT of whole image (inset). Lattice fringes are continuous across striation boundaries.

Figure 10. Percentage of Mn(III) and of Mn(II) relative to the total Mn as determined by X-ray photoelectron spectroscopy. Hashed lines represent morphotropic phase boundaries that separate triclinic from hexagonal birnessites. Data from Ilton et al. (2016) and this study.

Table 1a. Rietveld refinement results of unit cell parameters for Ca-exchanged birnessite

pH	**Ca^{2+} (M)**	**Time**	**a (Å)**	**b (Å)**	**c (Å)**	**α (°)**	**β (°)**	**γ (°)**
7.5[*]	0.1	1 day	5.113(1)	2.828(1)	7.009(1)	94.90(1)	89.94(1)	89.55(1)
7.5[*]	0.01	1 day	5.136(2)	2.832(1)	7.047(3)	94.73(2)	90.27(3)	89.77(2)
6.5	1.0	2 min	5.137(1)	2.828(1)	7.009(1)	94.93(1)	90.48(1)	89.78(1)
6.5	1.0	20 days	5.135(1)	2.826(1)	7.043(1)	94.80(1)	90.40(1)	89.77(1)
5.5	1.0	1 day	5.136(1)	2.826(1)	7.035(1)	95.01(1)	90.40(1)	89.79(1)
4.0	1.0	1 day	5.135(1)	2.825(1)	7.045(1)	94.97(1)	90.49(1)	89.84(1)
3.0	1.0	1 day	5.139(1)	2.829(1)	7.032(1)	94.81(1)	90.43(1)	89.82(1)
3.0 38%	0.1	1 day	5.173(1)	2.845(1)	7.154(1)	95.98(1)	90.64(1)	89.90(1)
62%			2.835(1)		7.258(1)			
3.0 24%	0.01	1 day	5.132(1)	2.809(1)	7.031(1)	95.62(1)	90.67(1)	90.13(1)
76%			2.817(1)		7.139(1)			
2.0[*]	0.1	1 day	4.919(1)	2.863(1)	7.358(1)	94.25(1)	92.99(1)	90.12(1)
2.0[*]	0.01	1 day	2.8592(4)		7.368(1)			

Table 1b. Rietveld refinement results of unit cell parameters for Na-birnessite (this study), Hexagonal-birnessite (this study), Li-birnessite (unpublished results), K-birnessite (Lopano et al. 2007), Ba-birnessite (Lopano et al. 2007), Mg-birnessite (unpublished results), Cs-birnessite (Lopano et al 2009).

	a (Å)	**b (Å)**	**c (Å)**	**α (°)**	**β (°)**	**γ (°)**
Na-birnessite (this study)	5.176(4)	2.848(6)	7.310(3)	89.18(6)	103.26(8)	89.76(4)
Hexagonal-birnessite (this study)	2.820(8)		7.267(5)			
Li-birnessite *	5.1401(4)	2.8424(2)	7.1598(8)	90.04(3)	103.109(8)	90.01(2)
K-birnessite (Lopano et al. 2007)	5.1371(5)	2.8476(2)	7.2129(8)	89.95(1)	100.74(7)	89.704(9)
Ba-birnessite (Lopano et al. 2007)	5.1713(5)	2.8473(9)	7.3039(6)	89.533(8)	102.968(3)	89.903(7)
Mg-birnessite *	5.022(1)	2.842(1)	7.041(2)	89.81(2)	96.11(2)	89.89(2)
Cs-birnessite (Lopano et al 2009)	5.1298(4)	2.8445(6)	7.5029(7)	90.12(3)	101.395(7)	89.958(7)

*unpublished result

Table 2. X-ray Photoelectron Spectroscopy (XPS) results.

	Mn^{4+} (%)	**Mn^{3+} (%)**	**Mn^{2+} (%)**	**Average Oxidation State**
Ca-birnessite 0.1M pH 7.5	64 (4)	29 (5)	7 (1)	3.57 (3)
Ca-birnessite 0.01M pH 3	67 (4)	22 (9)	11 (5)	3.55 (3)
Ca-birnessite 0.01M pH 2	68 (1)	21 (2)	11 (3)	3.58 (3)

Note: Errors are 3σ

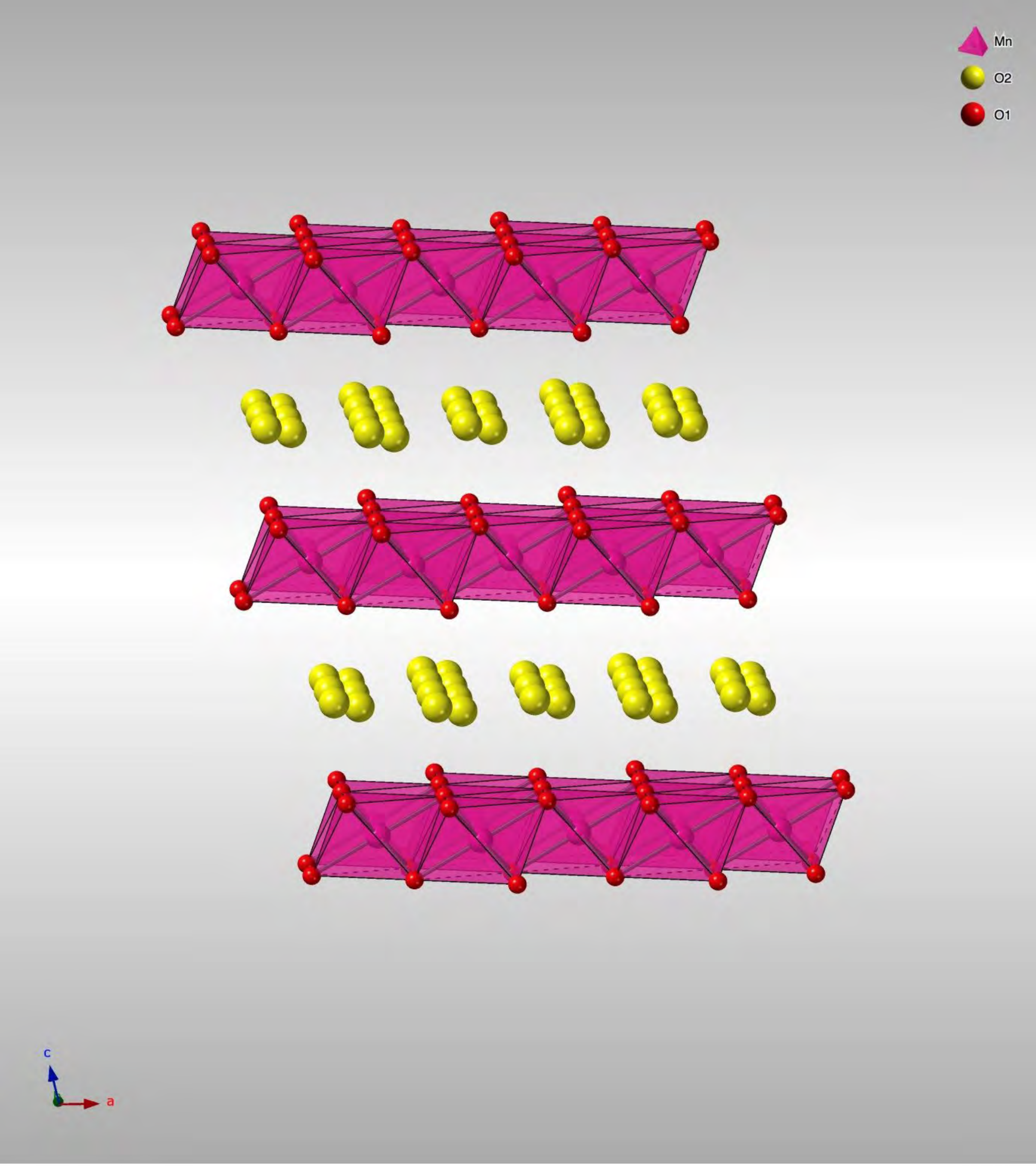

Figure 1a

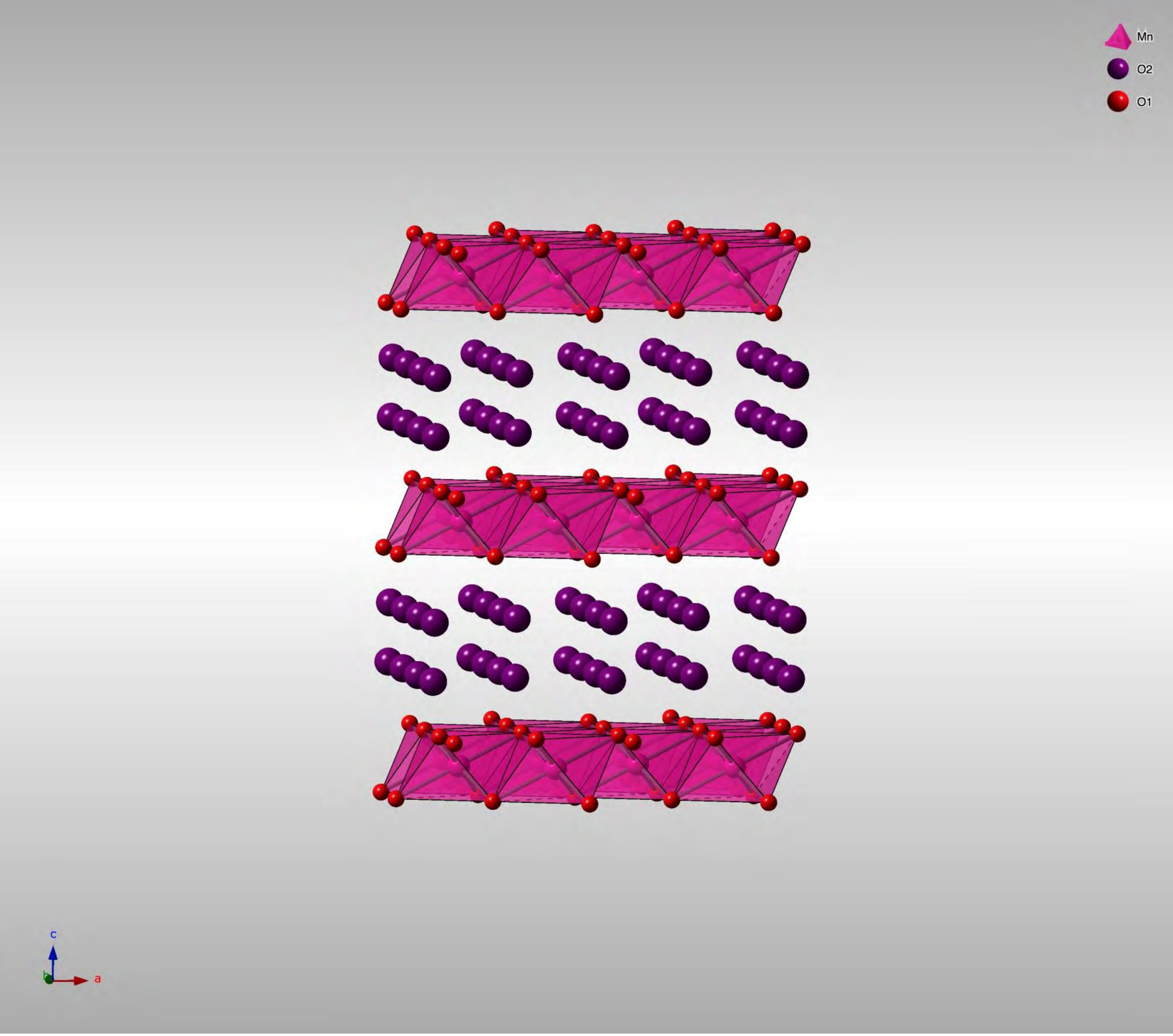

Figure 1b

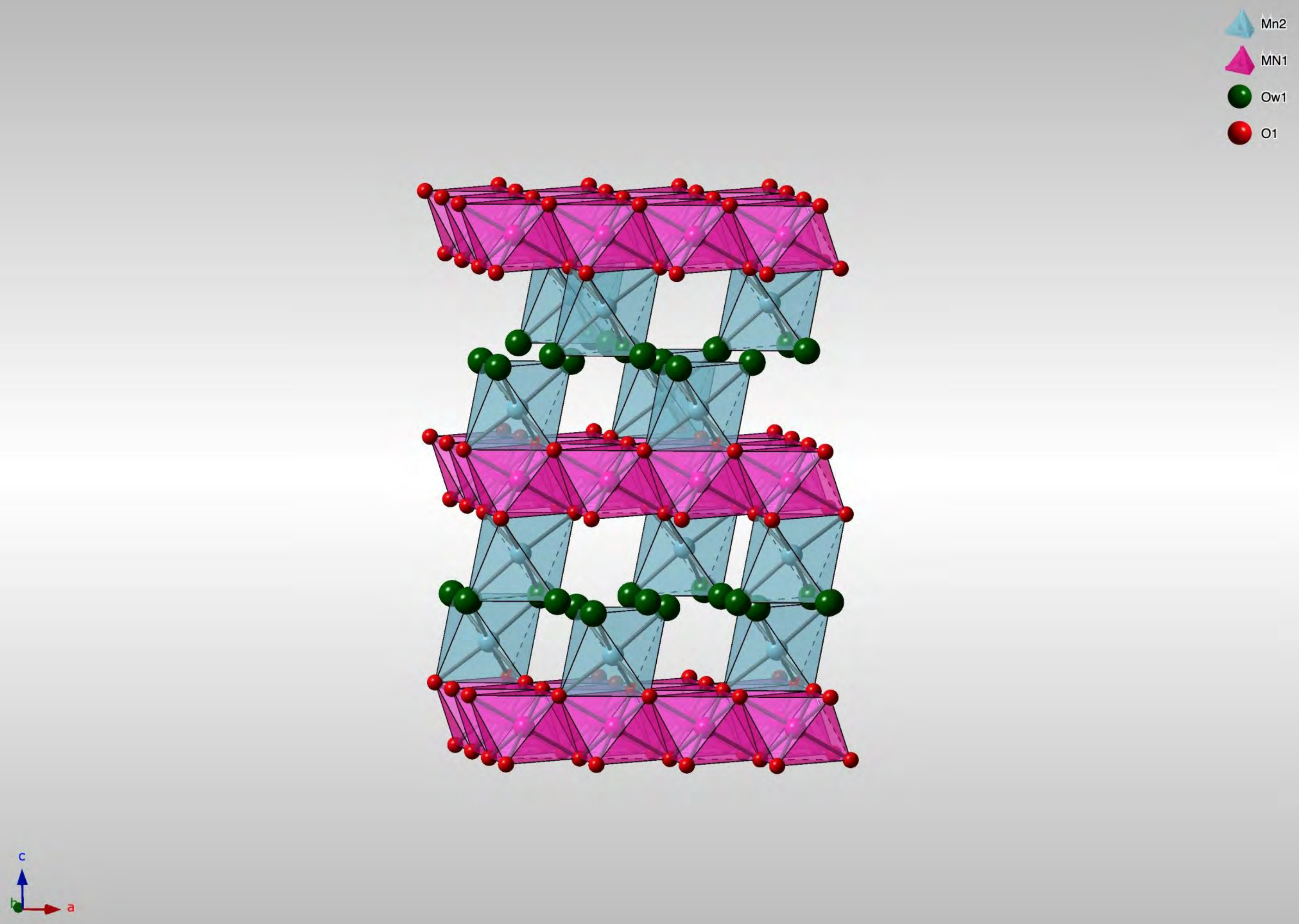

Figure 1c

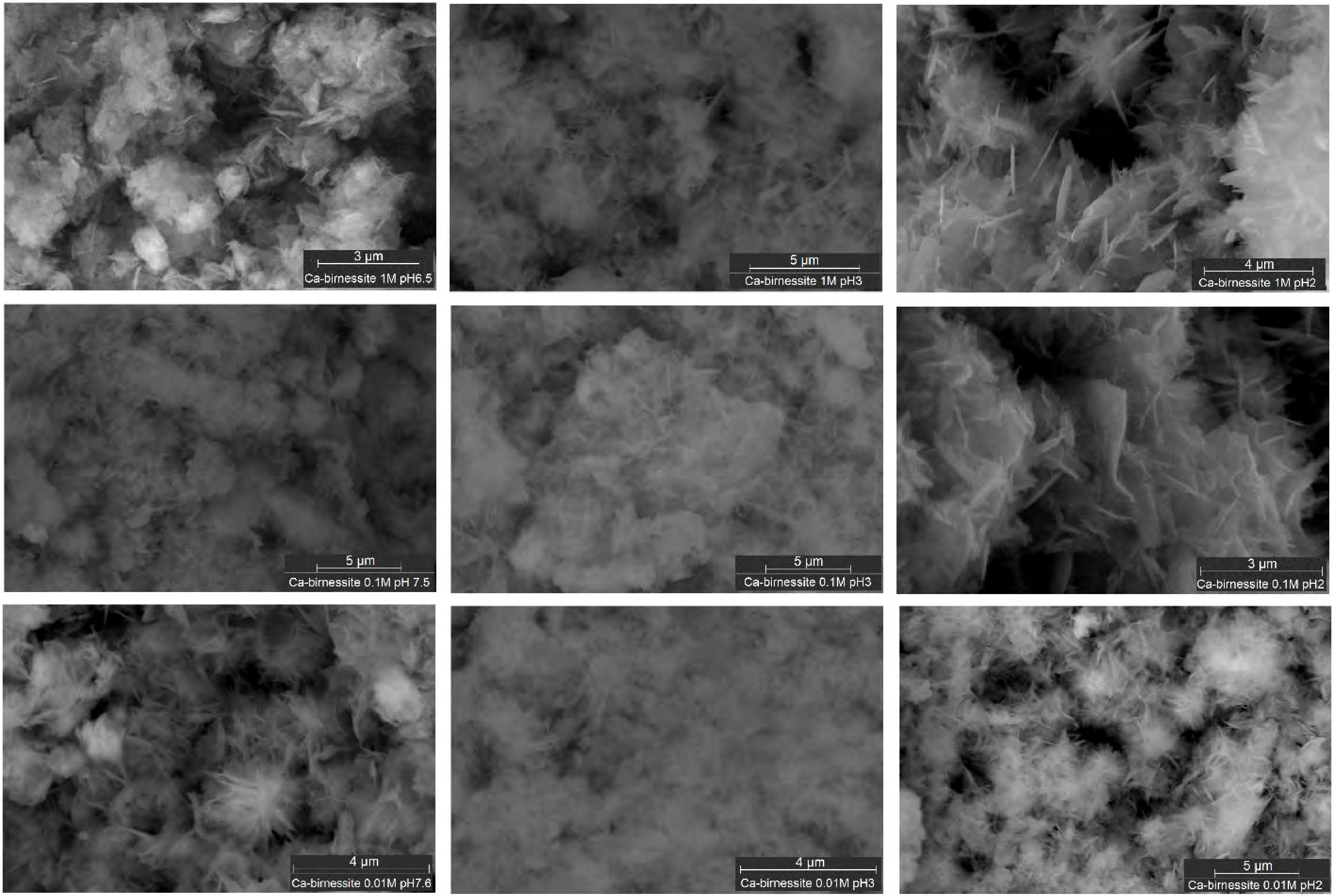
3 μm
Ca-birnessite 1M pH6.5
5 μm
Ca-birnessite 1M pH3
4 μm
Ca-birnessite 1M pH2
5 μm
Ca-birnessite 0.1M pH 7.5
5 μm
Ca-birnessite 0.1M pH3
3 μm
Ca-birnessite 0.1M pH2
4 μm
Ca-birnessite 0.01M pH7.6
4 μm
Ca-birnessite 0.01M pH3
5 μm
Ca-birnessite 0.01M pH2

Figure 2

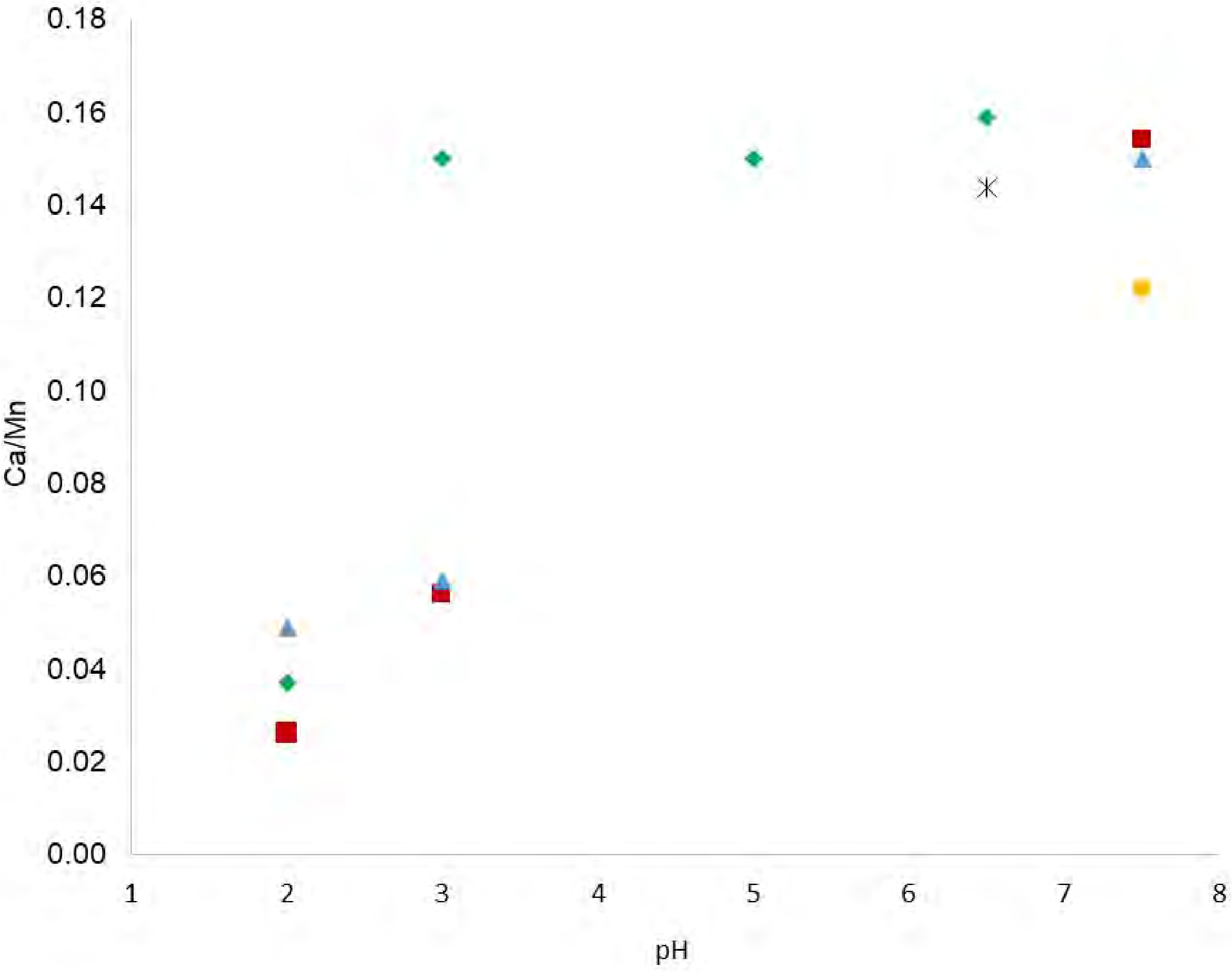

Figure 3

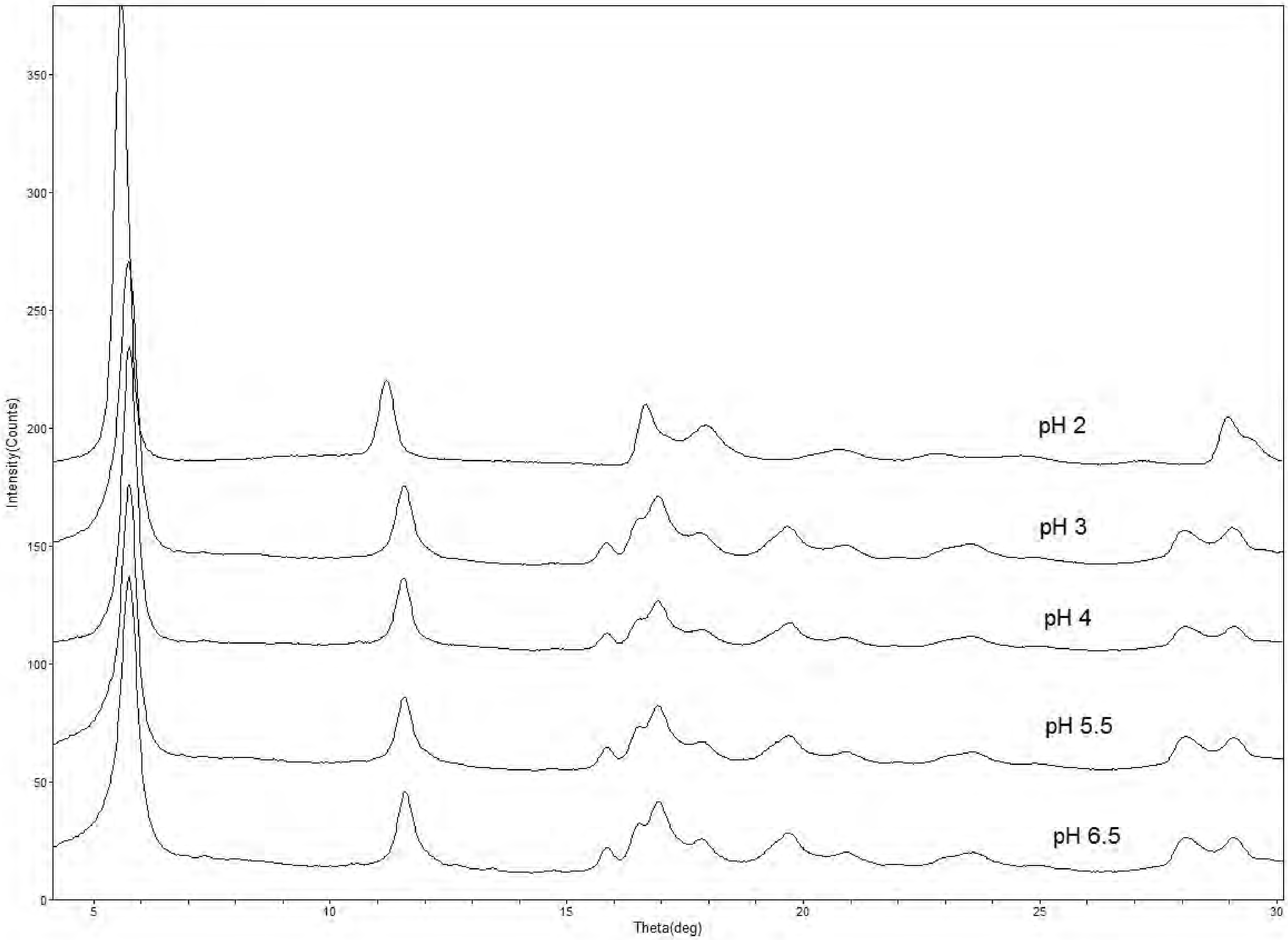
Intensity(Counts)
350
300
250
200
150
100
50
0
5
10
15
20
25
30
Theta(deg)
pH 2
pH 3
pH 4
pH 5.5
pH 6.5

Figure 4

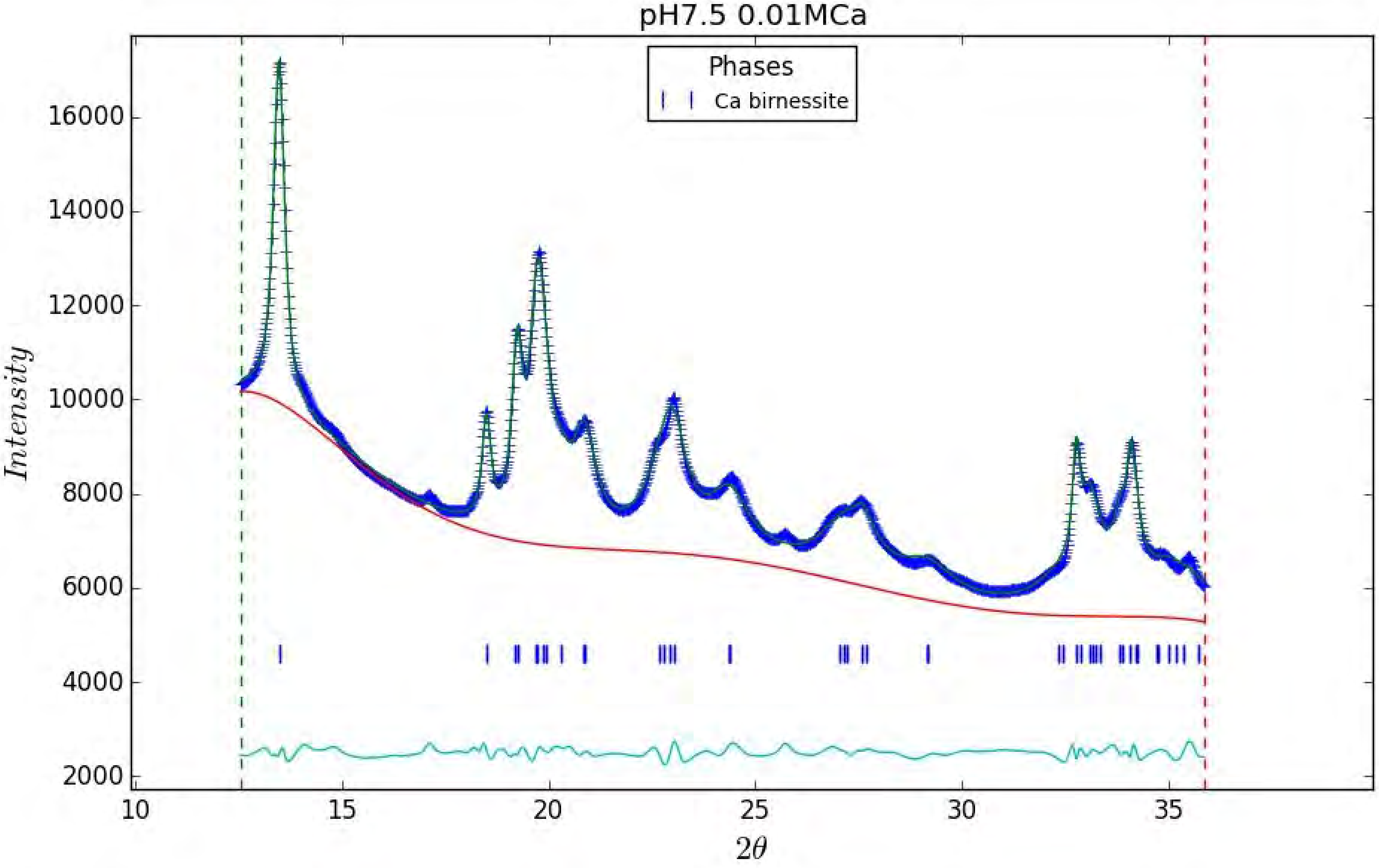
pH7.5 0.01MCa
Phases
Ca birnessite
Intensity
2θ
16000
14000
12000
10000
8000
6000
4000
2000
10
15
20
25
30
35

Figure 5a

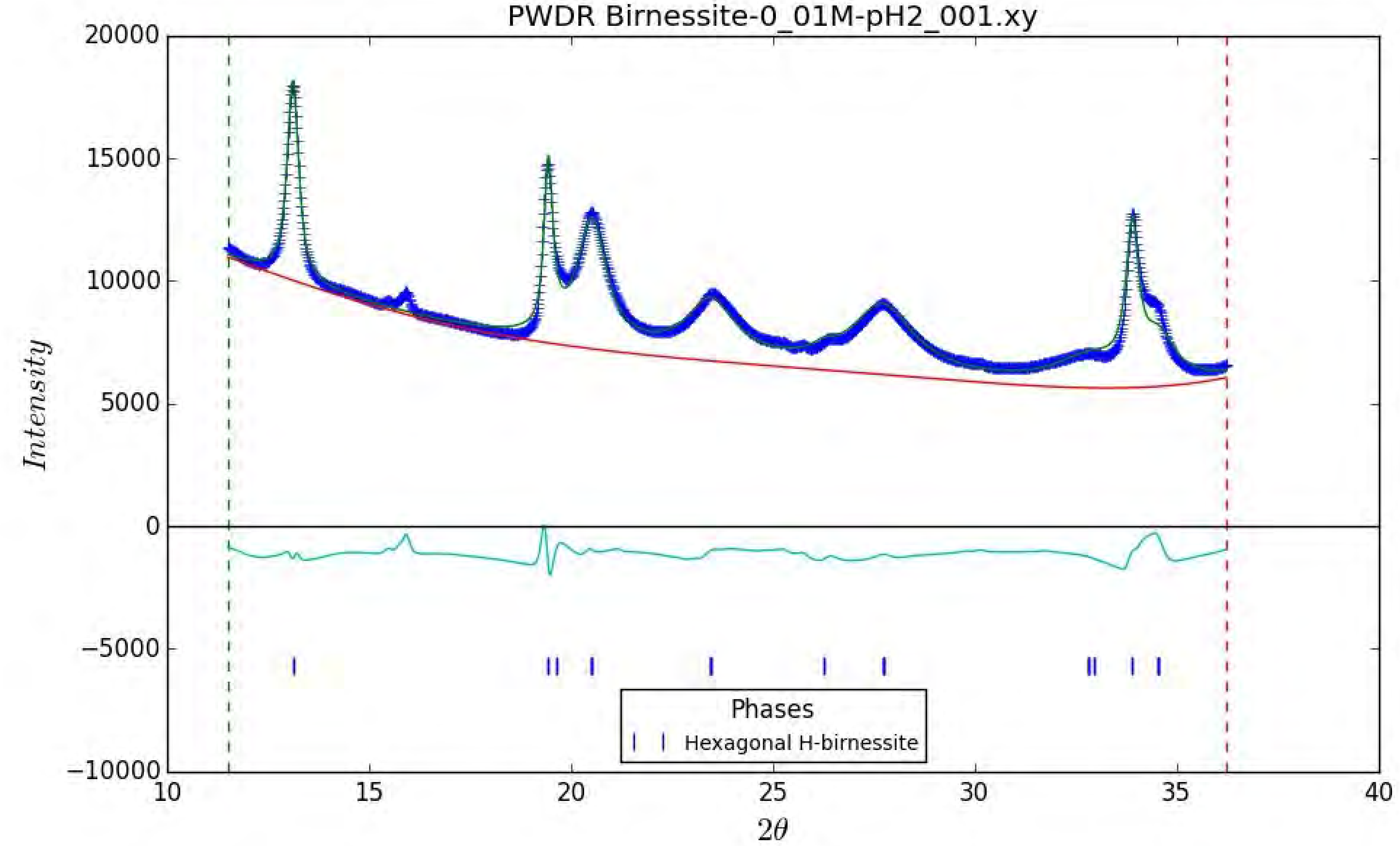
PWDR Birnessite-0_01M-pH2_001.xy
Intensity
20000
15000
10000
5000
0
−5000
−10000
10
15
20
25
30
35
40
2θ
Phases
Hexagonal H-birnessite

Figure 5b

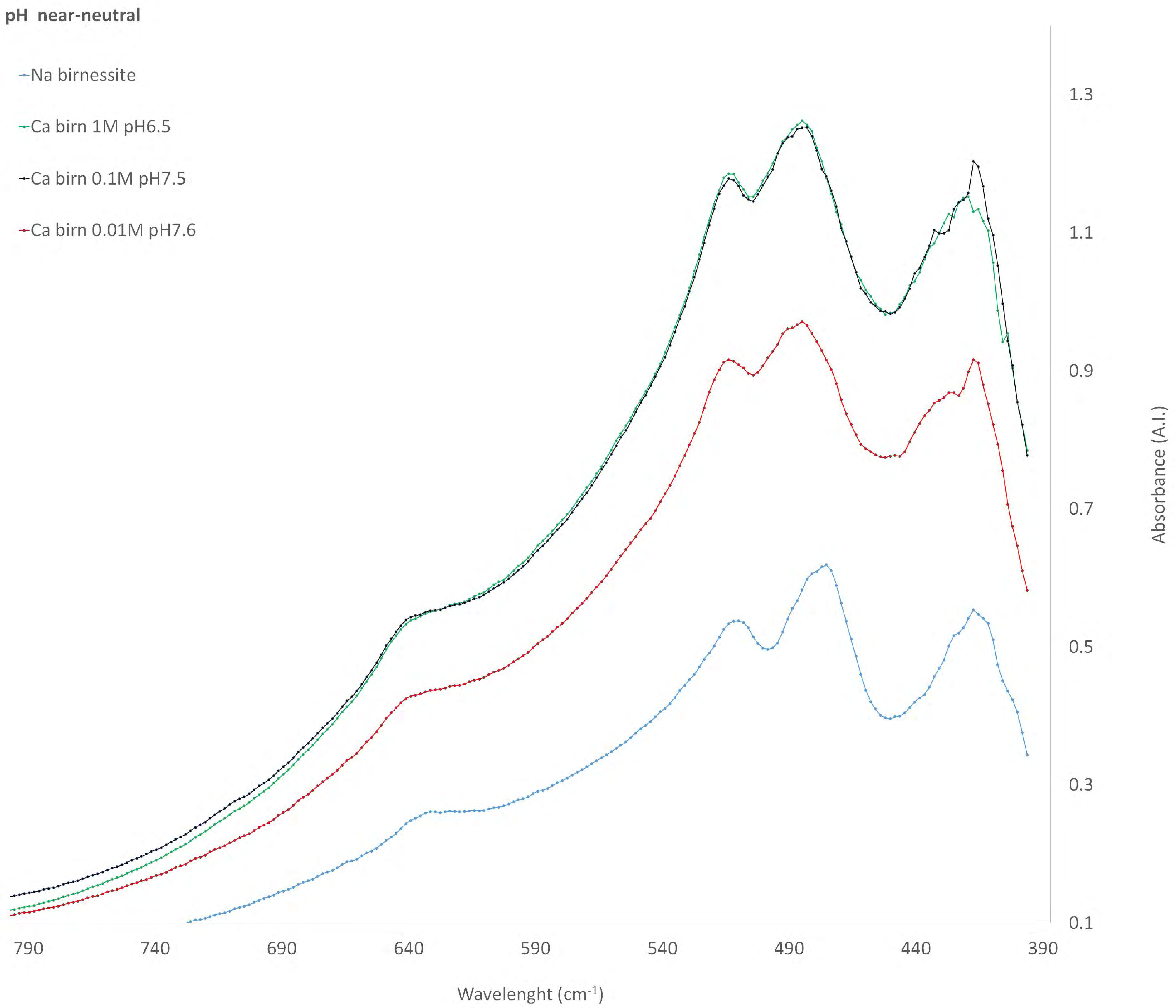
pH near-neutral
Na birnessite
Ca birn 1M pH6.5
Ca birn 0.1M pH7.5
Ca birn 0.01M pH7.6
1.3
1.1
0.9
0.7
0.5
0.3
0.1
Absorbance (A.I.)
790
740
690
640
590
540
490
440
390
Wavelenght (cm-1)

Figure 6a

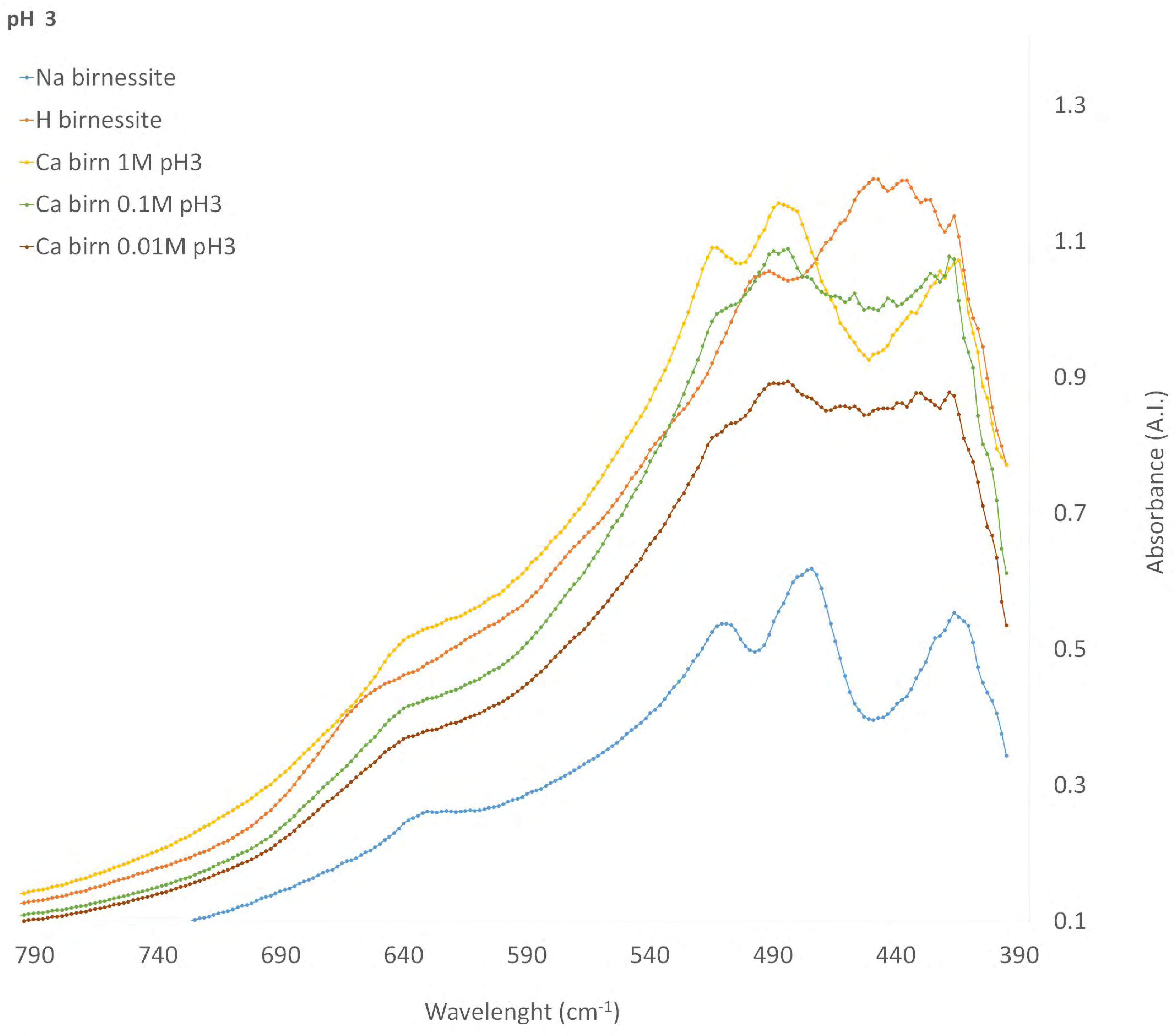
pH 3
Na birnessite
H birnessite
Ca birn 1M pH3
Ca birn 0.1M pH3
Ca birn 0.01M pH3
1.3
1.1
0.9
0.7
0.5
0.3
0.1
Absorbance (A.I.)
790
740
690
640
590
540
490
440
390
Wavelenght (cm-1)

Figure 6b

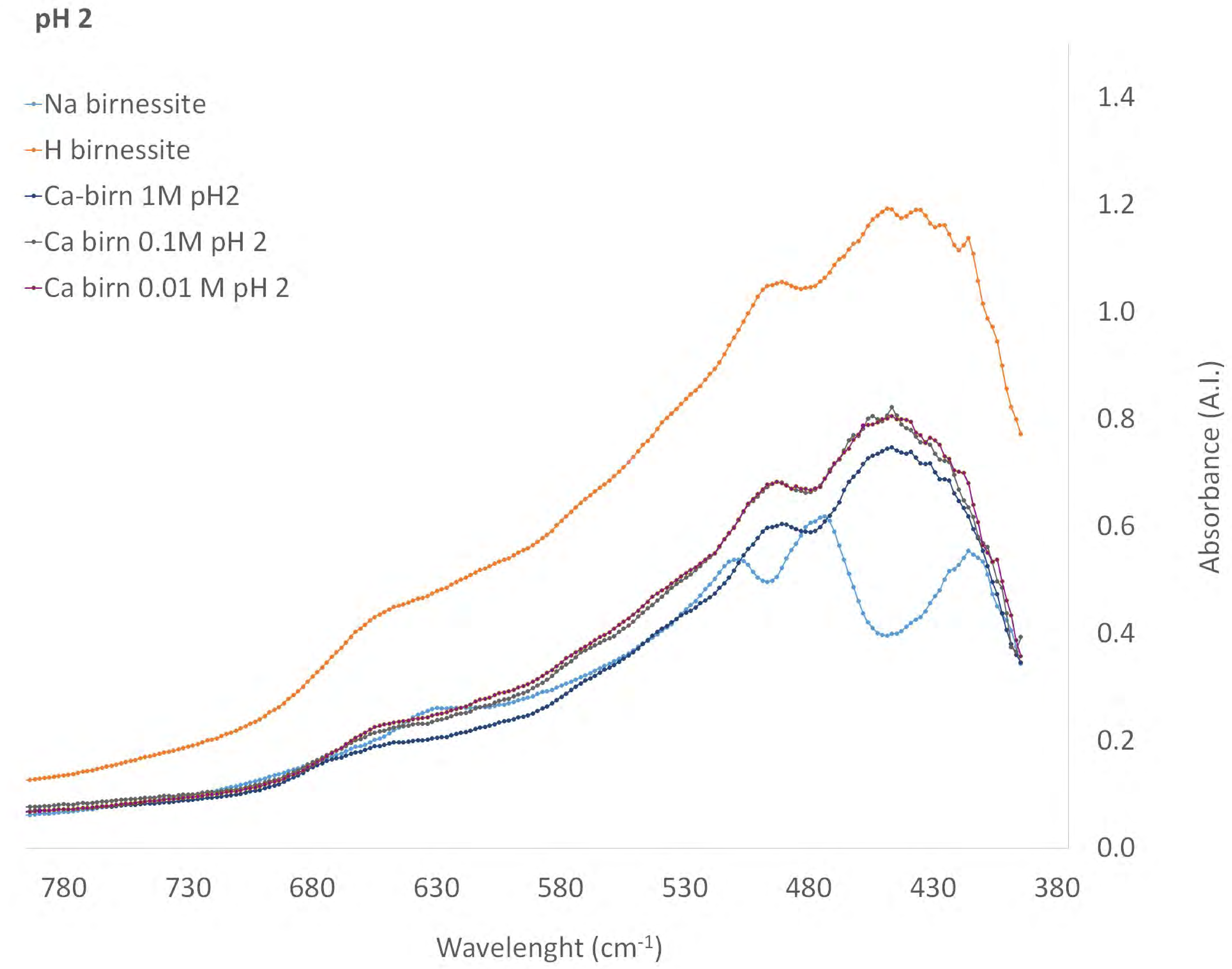
pH 2
Na birnessite
H birnessite
Ca-birn 1M pH2
Ca birn 0.1M pH 2
Ca birn 0.01 M pH 2
1.4
1.2
1.0
0.8
0.6
0.4
0.2
0.0
Absorbance (A.I.)
780
730
680
630
580
530
480
430
380
Wavelenght (cm-1)

Figure 6c

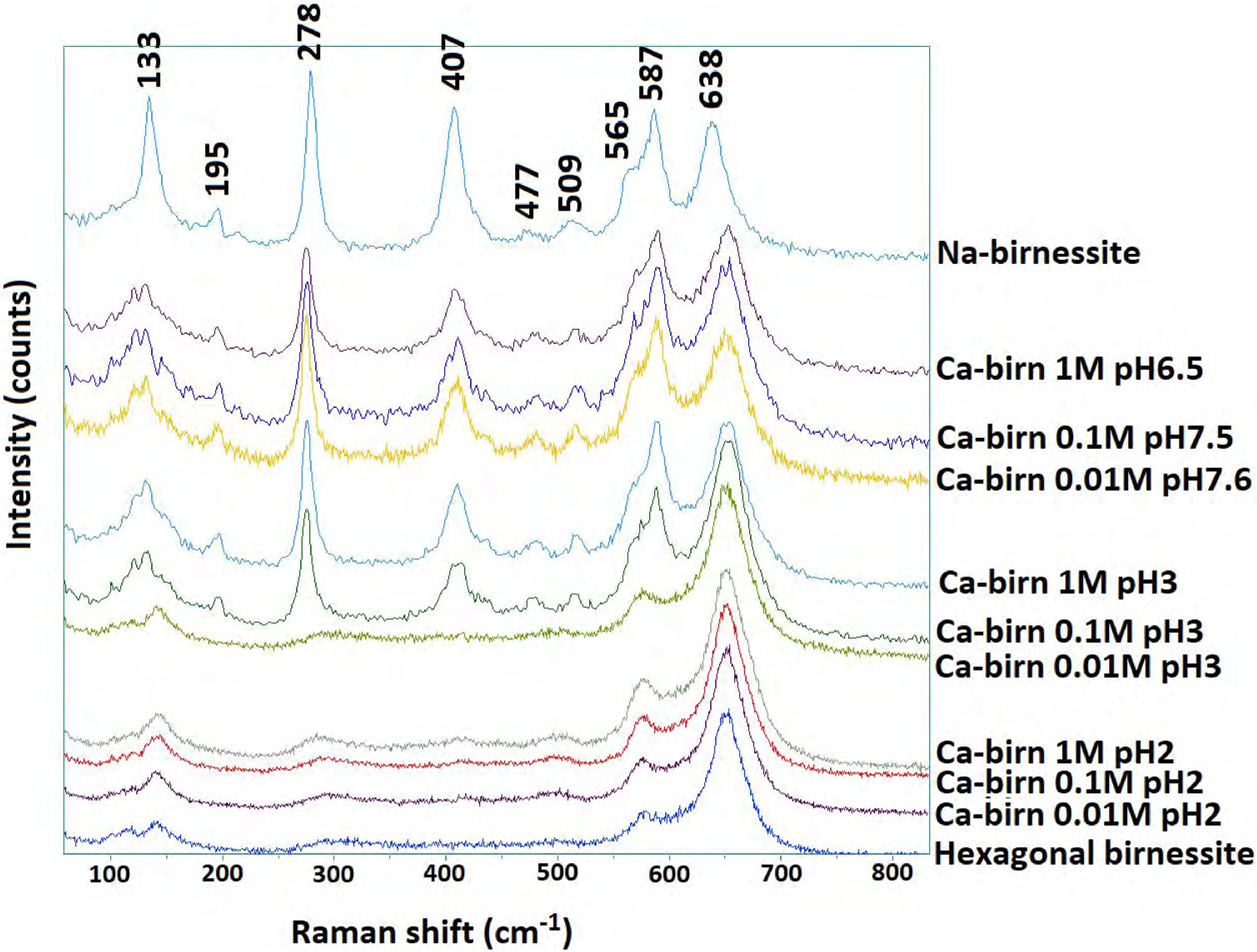
133
195
278
407
477
509
565
587
638
Na-birnessite
Ca-birn 1M pH6.5
Ca-birn 0.1M pH7.5
Ca-birn 0.01M pH7.6
Ca-birn 1M pH3
Ca-birn 0.1M pH3
Ca-birn 0.01M pH3
Ca-birn 1M pH2
Ca-birn 0.1M pH2
Ca-birn 0.01M pH2
Hexagonal birnessite
Intensity (counts)
100
200
300
400
500
600
700
800
Raman shift (cm^{-1})

Figure 7

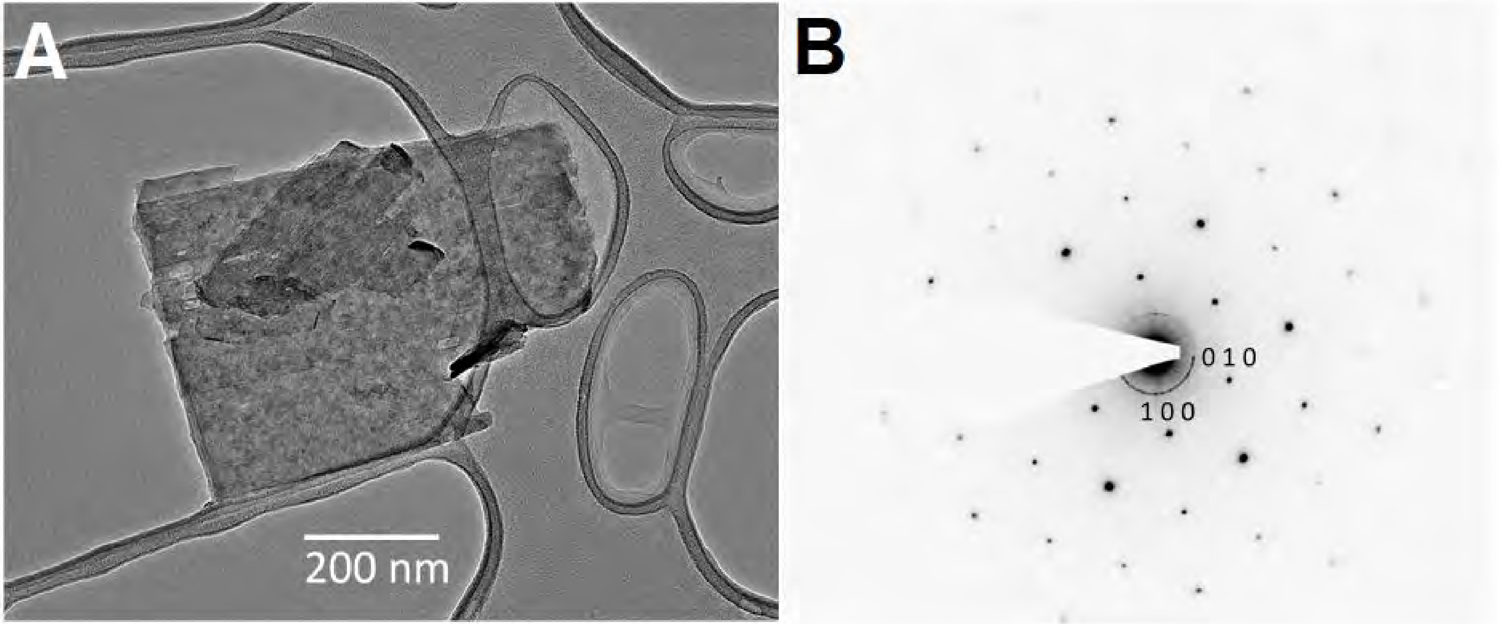

Figure 8a, b

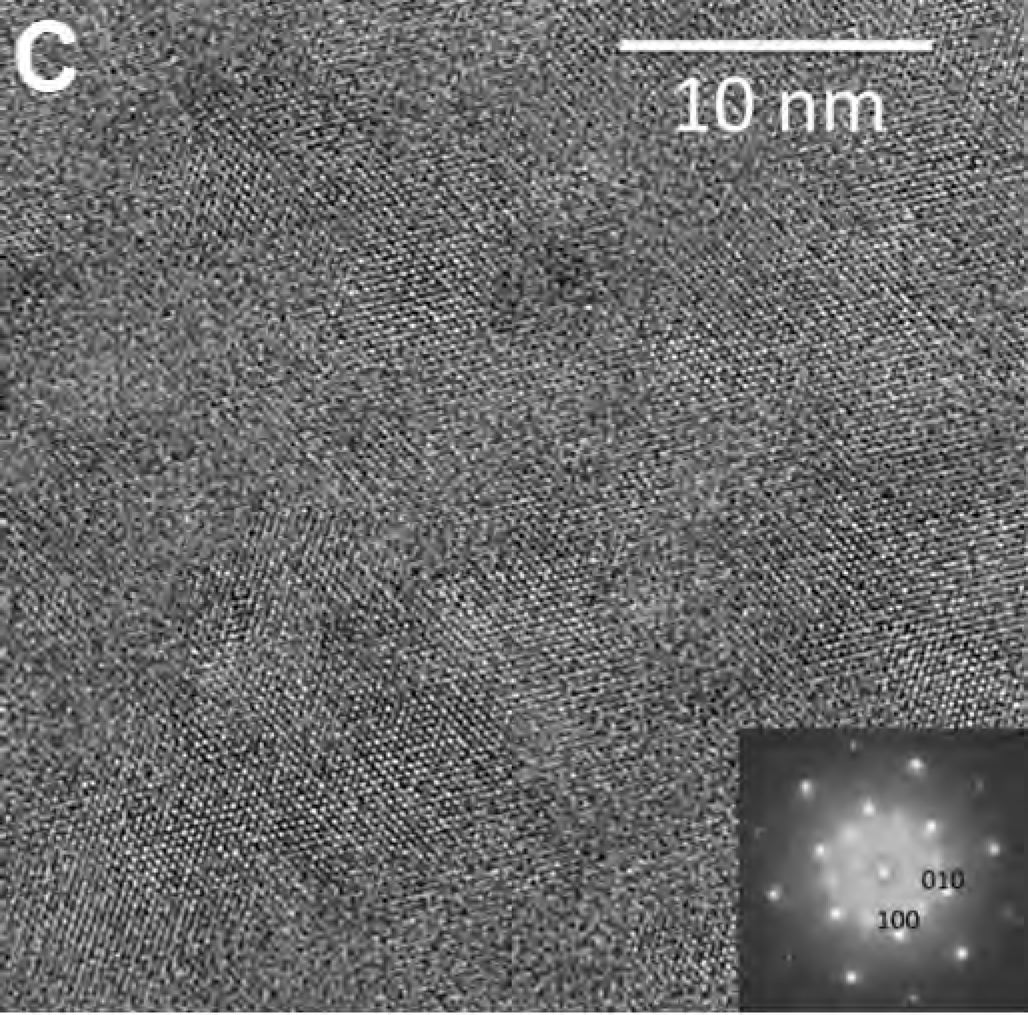

Figure 8c

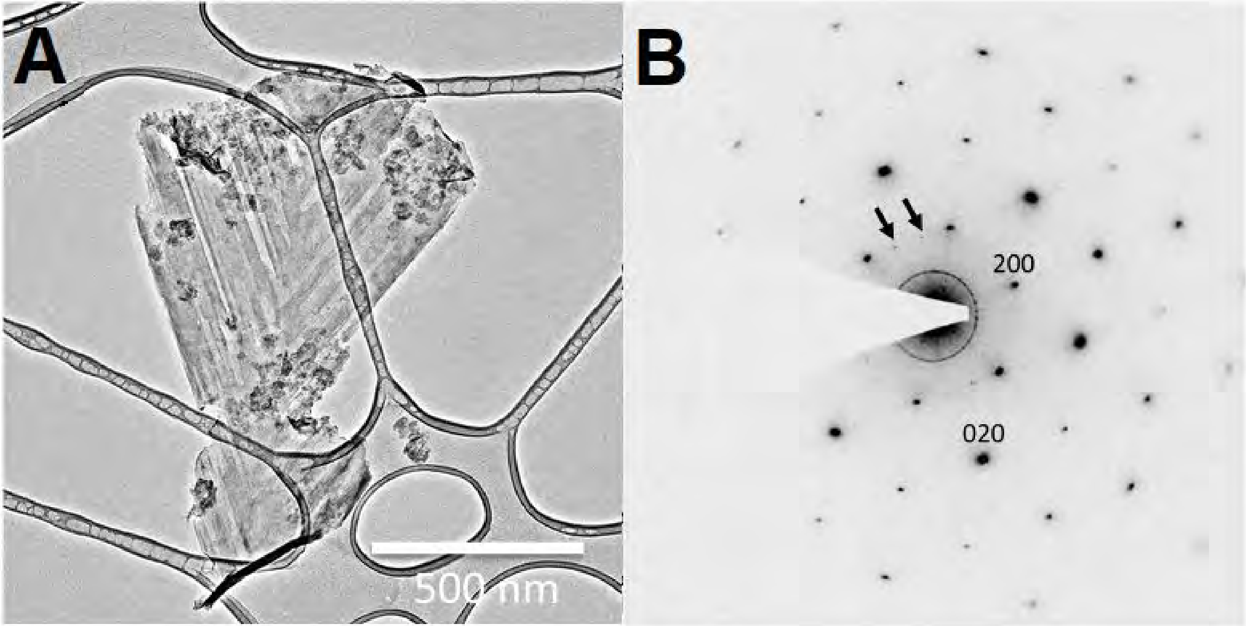

Figure 9a, b

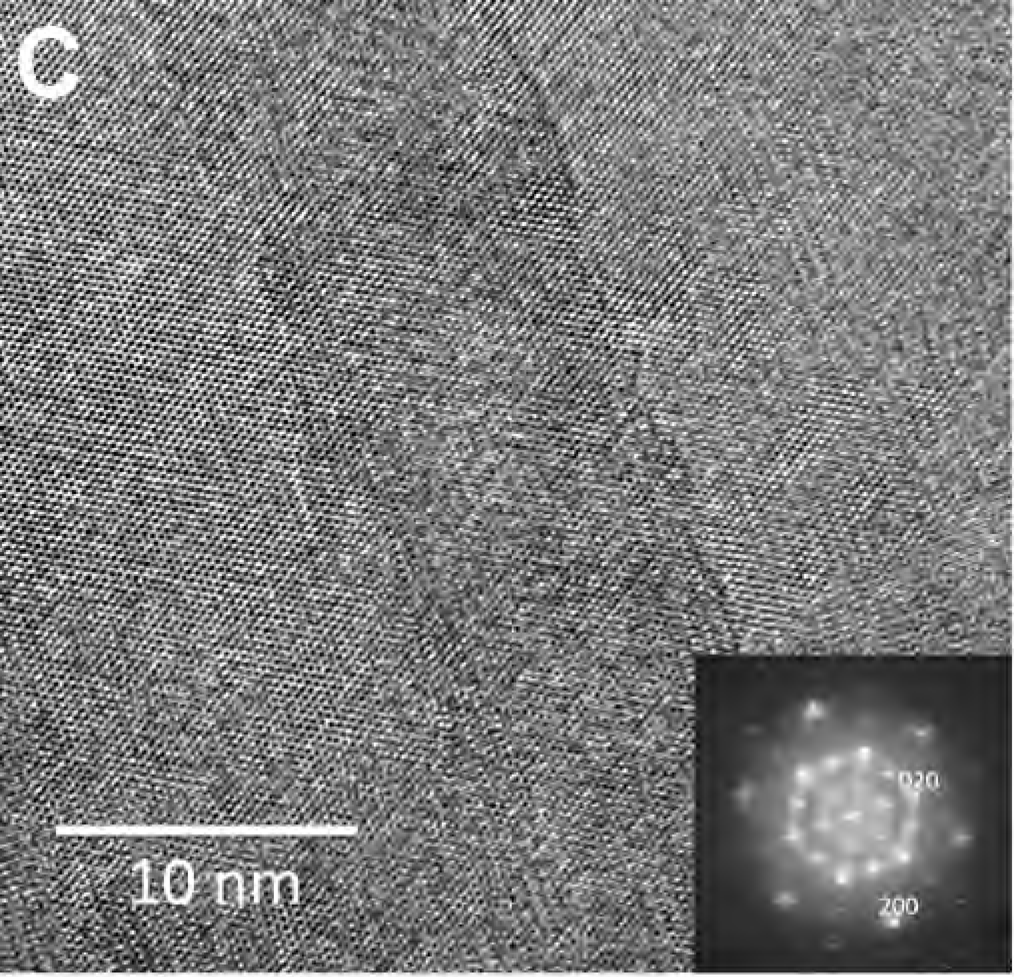

Figure 9c

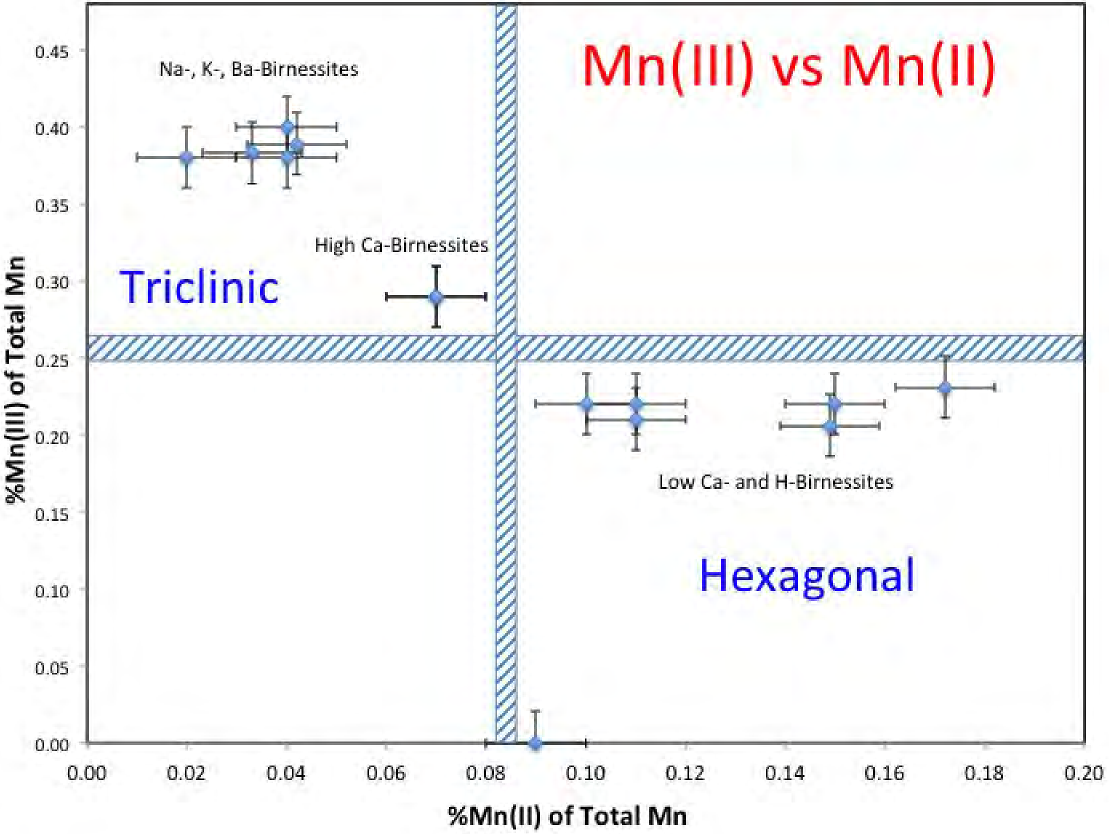
Mn(III) vs Mn(II)
Na-, K-, Ba-Birnessites
High Ca-Birnessites
Triclinic
Low Ca- and H-Birnessites
Hexagonal
%Mn(III) of Total Mn
%Mn(II) of Total Mn
0.45
0.40
0.35
0.30
0.25
0.20
0.15
0.10
0.05
0.00
0.00
0.02
0.04
0.06
0.08
0.10
0.12
0.14
0.16
0.18
0.20

Figure 10